Polyphenolic Boronates Inhibit Tumor Cell Proliferation: Potential Mitigators of Oxidants in the Tumor Microenvironment

Gang Cheng, Hakim Karoui, Micael Hardy, Balaraman Kalyanaraman

cancers

MDPI

Article

Polyphenolic Boronates Inhibit Tumor Cell Proliferation: Potential Mitigators of Oxidants in the Tumor Microenvironment

Gang Cheng [1], Hakim Karoui [2], Micael Hardy [2] and Balaraman Kalyanaraman [1,*]

[1] Department of Biophysics, Medical College of Wisconsin, Milwaukee, WI 53226, USA
[2] Aix Marseille Univ, CNRS, ICR, 13009 Marseille, France
* Correspondence: balarama@mcw.edu

Simple Summary: Several plant-based compounds inhibit tumor cell growth. Selective modification of these compounds significantly increases their antitumor potency. The goal of this study was to develop less toxic, more potent natural compounds for use in cancer and immune therapies. To this end, we modified the structures of honokiol and magnolol, the two active components of magnolia extract. The modified compounds—honokiol boronate and mitochondria-targeted honokiol boronate—target the mitochondria of tumor cells and inhibit cell proliferation. These boronate derivatives also react with oxidants that are generated in tumor mitochondria and the tumor microenvironment. During this process, these boronate derivatives are also converted back to the original compounds with antitumor potencies. Thus, boronation of naturally occurring plant-derived compounds could make them more active in tumor cells as well as in the adjoining tumor microenvironment. These novel polyphenolic derivatives may enhance the scope of cancer immunotherapies.

Abstract: Boronate-based compounds have been used in brain cancer therapy, either as prodrugs or in combination with other modalities. Boronates containing pro-luminescent and fluorescent probes have been used in mouse models of cancer. In this study, we synthesized and developed polyphenolic boronates and mitochondria-targeted polyphenolic phytochemicals (e.g., magnolol [MGN] and honokiol [HNK]) and tested their antiproliferative effects in brain cancer cells. Results show that mitochondria-targeted (Mito) polyphenolic boronates (Mito-MGN-B and Mito-HNK-B) were slightly more potent than Mito-MGN and Mito-HNK in inhibiting proliferation of the U87MG cell line. Similar proliferation results also were observed in other cancer cell lines, such as MiaPaCa-2, A549 and UACC-62. Independent in vitro experiments indicated that reactive nitrogen species (e.g., peroxynitrite) and reactive oxygen species (e.g., hydrogen peroxide) stoichiometrically react with polyphenolic boronates and Mito-polphenolic boronates, forming polyphenols and Mito-polyphenols as major products. Previous reports suggest that both Mito-MGN and Mito-HNK activate cytotoxic T cells and inhibit immunosuppressive immune cells. We propose that Mito-polyphenolic boronate-based prodrugs may be used to inhibit tumor proliferation and mitigate oxidant formation in the tumor microenvironment, thereby generating Mito-polyphenols in situ, as well as showing activity in the tumor microenvironment.

Keywords: polyphenols; mitochondria; tumor microenvironment; boronates; reactive and nitrogen species

Citation: Cheng, G.; Karoui, H.; Hardy, M.; Kalyanaraman, B. Polyphenolic Boronates Inhibit Tumor Cell Proliferation: Potential Mitigators of Oxidants in the Tumor Microenvironment. *Cancers* **2023**, *15*, 1089. https://doi.org/10.3390/cancers15041089

Academic Editors: Elisabetta Ferretti and Marco Tafani

Received: 21 December 2022
Revised: 31 January 2023
Accepted: 1 February 2023
Published: 8 February 2023

1. Introduction

Boronates are a novel class of molecules containing an electron-deficient boron atom. Borax and boronophenylalanine have been used in boron neutron capture therapy (BNCT) to treat glioma [1–5]. There is extensive literature indicating the antiproliferative and

antitumor effects of several boron-containing compounds in various cancers [6–12]. In some studies, boronates are used as prodrugs, releasing the active antitumor drug in situ, which occurs following its reaction with hydrogen peroxide (H_2O_2) [6–11]. Boronate-based fluorophores and positron-emission tomography (PET) active compounds have been in cancer cells and cancer xenografts in the detection of oxidants [13–16].

From a chemical viewpoint, it has been known for decades that boronates react stoichiometrically yet slowly ($k = 1\ M^{-1}s^{-1}$) with H_2O_2, forming the corresponding hydroxyl product [17]. Boron is electron-deficient and a weak Lewis acid. We and others have shown that biologically relevant proinflammatory oxidants such as peroxynitrite ($ONOO^-$), hypochlorous acid (HOCl), and H_2O_2 undergo a nucleophilic addition reaction with phenylboronates and stoichiometrically form the corresponding phenol as a major product [13,18–26]. An interesting finding is that $ONOO^-$ reacts nearly a million times faster with boronates than H_2O_2 [18,27,28]. Based on the rate constant determinations, boronates can compete very effectively with other biological reductants, such as glutathione, in their ability to scavenge $ONOO^-$ [18].

There is increasing interest in understanding the role of oxidant formation and nitrosative stress in immunosuppressive tumor microenvironment (TME) [29–39]. Mitigating nitrosative stress has been reported to activate cytotoxic T cells involved in killing tumor cells [40]. Inhibition of cytokine nitration induced by reactive nitrogen species eliminated T cell exhaustion [41]. Reports also suggest that enhancing oxidant formation is critical for enhancing immunotherapy [35]. The paradoxical role of oxidative stress is discussed in relation to drug resistance in cancer [42].

In this study, we conjugated the boronate moiety to naturally occurring polyphenolic compounds and their mitochondria-targeted analogs (Figure 1). These boronate-based polyphenolics react with proinflammatory oxidants such as $ONOO^-$, HOCl, and H_2O_2, and generate the original compounds in situ. These polyphenolics exert an anti-immune and antitumor function. In some cases, polyphenolic boronates themselves exhibit more potency than the parent polyphenolics. In addition, these compounds can stoichiometrically scavenge reactive oxygen and nitrogen species generated in tumors and in the TMEs from immune cells (e.g., neutrophils, macrophages). We surmise that a molecule incorporating the oxidative phosphorylation (OXPHOS)-inhibiting drug group attached to a boronate could decrease T cell exhaustion through scavenging of nitric oxide-derived oxidants released in the TME, thereby generating a polyphenolic mitochondria-targeted drug (MTD) with antitumor function. Here, we describe the results of polyphenolic boronates in glioblastoma, lung cancer, melanoma, and pancreatic cancer cell lines. The corresponding mitochondria-targeted polyphenols (mitochondria-targeted honokiol [Mito-HNK] and mitochondria-targeted magnolol [Mito-MGN]) have previously been tested in these cancer cells [43,44].

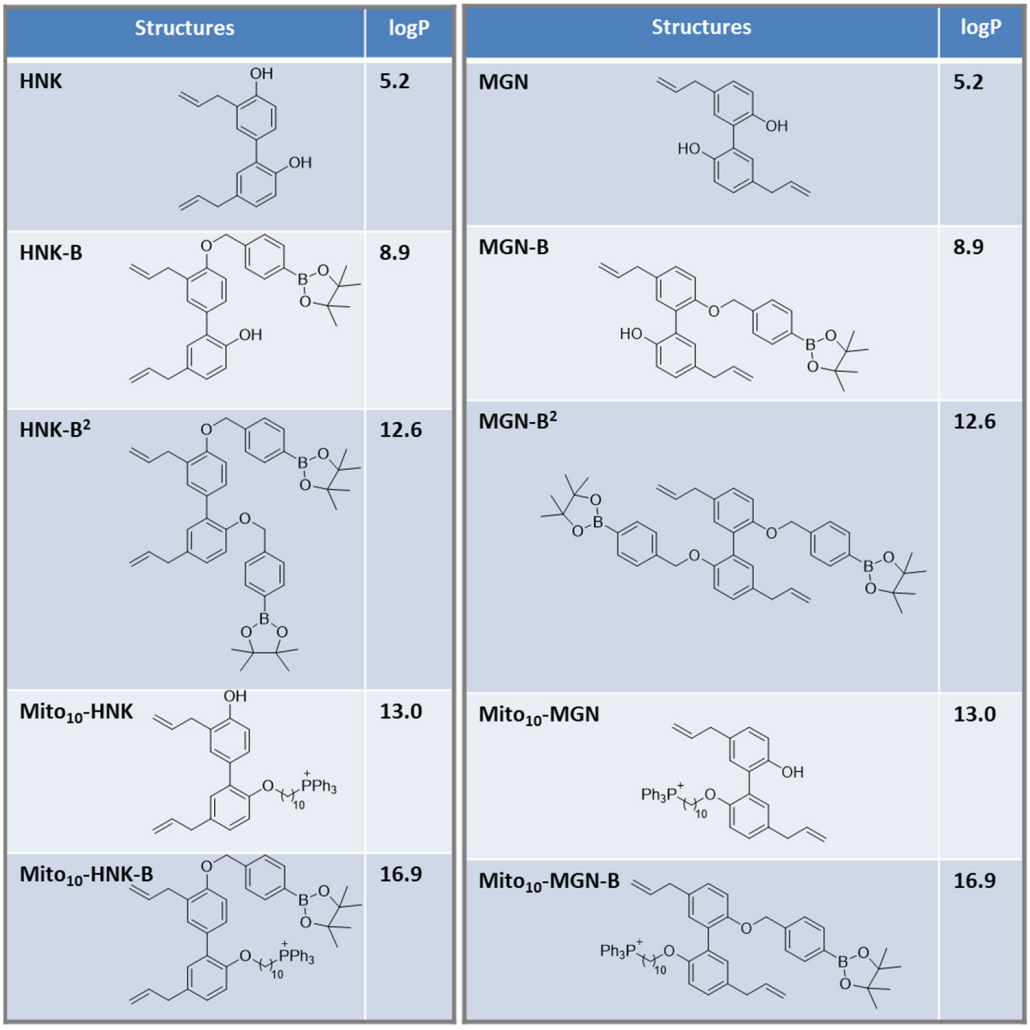

Figure 1. Structures of selected polyphenolic boronates and polyphenols, and the calculated values of the octanol/water partition coefficients.

2. Materials and Methods

All chemicals and organic solvents were commercially available and were used as supplied. The reactions were monitored by thin layer chromatography (TLC) using silica gel Merck ^{60}F254. Crude materials were purified by flash chromatography on Merck silica gel 60 (0.040–0.063 mm). ^{31}P nuclear magnetic resonance (NMR), ^{1}H NMR, and ^{13}C NMR spectra were recorded with spectrometers at 400.13 MHz and 75.54 MHz, respectively. ^{1}H NMR spectra were recorded at 400.13 MHz using a Bruker DPX AVANCE 400 spectrometer equipped with a quattro nucleus probe. ^{1}H NMR and ^{31}P NMR were taken in deuterated chloroform ($CDCl_3$) using $CDCl_3$ and tetramethylsilane as internal references, respectively. Chemical shifts (δ) are reported in ppm and J values in hertz. Synthetic procedures for preparing polyphenolic and Mito-polyphenolic boronates are shown in Schemes 1–5. NMR spectra are presented in Appendix A.

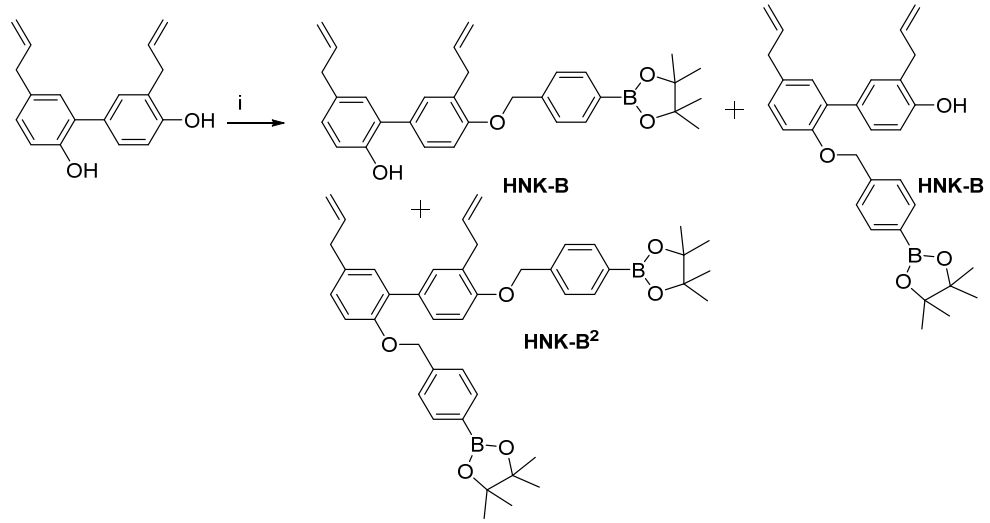

Scheme 1. Synthesis of HNK-B and HNK-B^2. Reagents and conditions: i, K_2CO_3, 2-(4-bromomethylphenyl)-4,4,5,5-tetramethyl-[1,3,2]-dioxaborolane, MeCN, reflux, 40%.

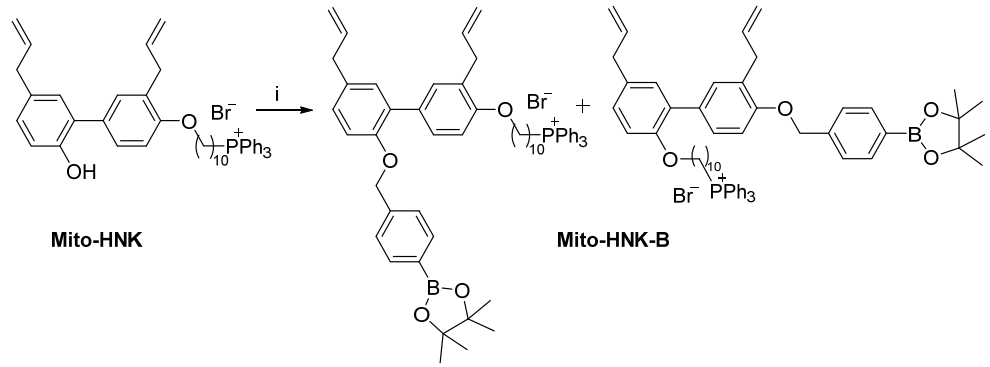

Scheme 2. Synthesis of Mito-HNK-B. Reagents and conditions: i, K_2CO_3, 2-(4-bromomethylphenyl)-4,4,5,5-tetramethyl-[1,3,2]-dioxaborolane, MeCN, reflux, 37%.

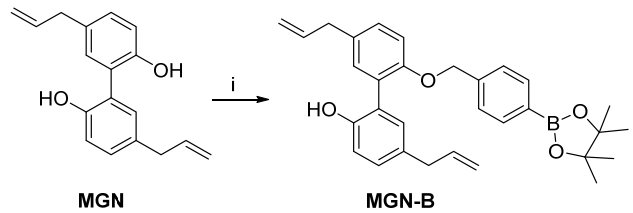

Scheme 3. Synthesis of MGN-B. Reagents and conditions: i, K_2CO_3, 2-(4-bromomethylphenyl)-4,4,5,5-tetramethyl-[1,3,2]-dioxaborolane, MeCN, reflux, 55%.

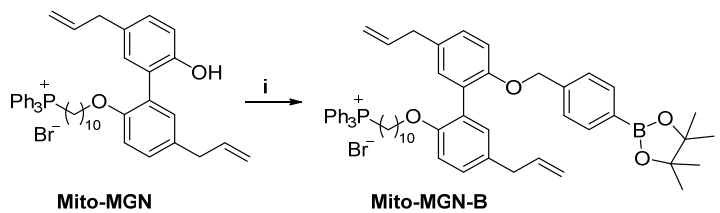

Scheme 4. Synthesis of Mito-MGN-B. Reagents and conditions: i, K_2CO_3, 2-(4-bromomethylphenyl)-4,4,5,5-tetramethyl-[1,3,2]-dioxaborolane, MeCN, reflux, 42%.

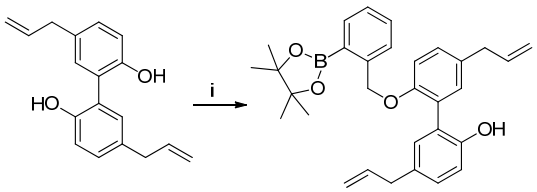

Scheme 5. Synthesis of MAG-BET. Reagents and conditions: i, K_2CO_3, 2-(2-bromomethylphenyl)-4,4,5,5-tetramethyl-[1,3,2]-dioxaborolane, MeCN, reflux, 27%.

2.1. Cell Culture

The U87MG (ATCC Cat# HTB-14, human glioblastoma cancer cells), A549 (ATCC Cat# CCL-185, human lung cancer cells), and MiaPaCa-2 (ATCC Cat# CRL-1420, human pancreatic cancer cells) cell lines were purchased from the American Tissue Culture Collection (Manassas, VA, USA). The UACC-62 melanoma cell line was purchased from AddexBio (San Diego, CA; Cat# C0020003). All cell lines were regularly authenticated. All cell lines were grown at 37 °C in 5% carbon dioxide. The U87MG, A549, and UACC-62 cells were maintained in Roswell Park Memorial Institute Medium 1640 medium (Thermo Fisher Scientific, Waltham, MA, USA; Cat# 11875) supplemented with 10% fetal bovine serum. MiaPaCa-2 cells were maintained in Dulbecco's Modified Eagle Medium (Thermo Fisher Scientific, Waltham, MA, USA; Cat# 11965) and supplemented with 10% fetal bovine serum. All cells were stored in liquid nitrogen and used within 20 passages after thawing.

2.2. Cell Proliferation

The IncuCyte Live-Cell Analysis System was used to continuously monitor cell proliferation, as described in earlier publications [43,45,46].

2.3. Synthesis of HNK-B and HNK-B^2

Honokiol boronate (HNK-B) and honokiol diboronate (HNK-B^2) were prepared by reacting honokiol (HNK) in the presence of 2-(4-bromomethylphenyl)-4,4,5,5-tetramethyl-[1,3,2]-dioxaborolane and potassium carbonate in acetonitrile (MeCN).

To a mixture of HNK (0.5 g, 1.92 mmol) and anhydrous potassium carbonate (0.34 g, 2.4 mmol) in MeCN (5 mL) was added 2-(4-bromomethylphenyl)-4,4,5,5-tetramethyl-[1,3,2]-dioxaborolane (0.57 g, 1.90 mmol). The mixture was stirred at reflux overnight. Then, ethyl acetate was added to the mixture as well as water (H2O) (20 mL). The organic layer was washed twice with H_2O and dried over sodium sulfate (Na_2SO_4). The solvent was removed under reduced pressure. Purification by flash chromatography (pentane/diethyl ether [Et_2O] 9/1 and 8/2) delivered the corresponding HNK-B as a mixture of two isomers (0.4 g, 43% yield) and HNK-B^2 (0.1 g, 7%). High-resolution mass spectrometry (HRMS) calculated for HNK-B $C_{31}H_{35}BO_4$ $[M+Na]^+$ 505.2526 returned 505.2526. HRMS calculated for HNK-B^2 $C_{44}H_{52}B_2O_6$ $[M+Na]^+$ 721.3857 returned 721.3855.

2.3.1. HNK-B

^{1}H NMR (400.13 MHz, $CDCl_3$) δ 7.83 (2H, 2d, *J* = 7.8, 7.8), 7.50–7.33 (3H, m), 7.25–7.12 (2H, m), 7.05–6.82 (3H, m), 6.09–5.94 (2H, m), 5.17 (2H,), 5.15–5.04 (5H, m), 3.48 (2H, 2d, *J* = 6.6, 6.3), 3.39–3.35 (2H, m), 1.36–1.37 (12H, 2s). ^{13}C NMR (75 MHz, $CDCl_3$) 156.1, 153.9, 153.2, 150.8, 140.5, 140.2, 137.8, 137.7, 136.5, 135.0, 134.9, 132.8, 132.1, 131.7, 131.2, 131.0, 130.7, 130.2, 130.1, 129.4, 129.0, 128.8, 127.9, 127.8, 126.3, 126.1, 124.7, 116.5, 115.9, 115.6, 115.5, 115.4, 113.5, 112.3, 83.9, 83.8, 70.6, 70.0, 39.4, 39.3, 35.2, 34.5, 29.7, 24.9.

2.3.2. HNK-B^2

^{1}H NMR (400.13 MHz, $CDCl_3$) δ 7.86 (2H, d, *J* = 7.8), 7.78 (2H, d, *J* = 7.8), 7.49 (2H, d, *J* = 7.8), 7.44 (1H, d, *J* = 1.8), 7.39–7.35 (3H, m), 7.15 (1H, d, *J* = 1.9), 7.06 (1H, dd, *J* = 8.3, 1.8), 6.93 (2H, dd, *J* = 8.3, 2.9), 6.07–5.92 (2H, m), 5.15 (2H, s), 5.13–5.04 (4H, m), 5.07 (2H, s), 3.49

(2H, d, J = 6.6), 3.37 (2H, d, J = 6.6), 1.37 (12H, s), 1.35 (12H, s). ^{13}C NMR (75 MHz, $CDCl_3$) δ 155.5, 153.9, 140.6, 140.5, 137.7, 136.9, 134.9, 134.8, 132.8, 131.3, 131.04, 131.02, 128.3, 128.3, 128.2, 127.8, 126.4, 126.1, 115.5, 113.4, 111.2, 83.8, 70.6, 69.9, 39.4, 34.6, 24.8.

2.4. Synthesis of Mito-HNK-B

Mitochondria-targeted honokiol boronate (Mito-HNK-B) was prepared by reacting Mito-HNK in the presence of 2-(4-bromomethylphenyl)-4,4,5,5-tetramethyl-[1,3,2]-dioxaborolane and potassium carbonate in MeCN.

To a mixture of Mito-HNK (0.36 g, 0.48 mmol) and anhydrous potassium carbonate (0.1 g, 0.7 mmol) in MeCN (5 mL) was added 2-(4-bromomethylphenyl)-4,4,5,5-tetramethyl-[1,3,2]-dioxaborolane (0.24 g, 0.7 mmol). The mixture was stirred at reflux overnight. Then, dichloromethane (CH_2Cl_2) was added to the reaction mixture as well as H_2O (20 mL). The organic layer was washed twice with H_2O and dried over Na_2SO_4. The solvent was removed under reduced pressure. The residue was washed with Et_2O. Purification by flash chromatography (from CH_2Cl_2 to CH_2Cl_2/ethanol [EtOH] 95/5) delivered the corresponding Mito-HNK-B as a mixture of two isomers as white solids (0.17 g, 37% yield). HRMS calculated for Mito-HNK-B $C_{59}H_{69}BBrO_4P$ $[M]^+$ 883.5031 returned 883.5028.

^{31}P (400.13 MHz, $CDCl_3$) δ 24.49, 24.46. ^{1}H NMR (400.13 MHz, $CDCl_3$) δ 7.90–7.64 (17H, m), 7.47–7.30 (4H, m), 7.16–7.00 (2H, m), 6.94–6.83 (2H, m), 6.07–5.90 (2H, m), 5.15–4.95 (6H, m), 3.88 (1H, t, J = 6.3), 3.90 (1H, t, J = 6.3), 3.85–3.73 (2H, m), 3.50–3.31 (4H, m), 1.82–1.68 (3H, m), 1.67–1.55 (5H,m), 1.35–1.34 (12H, 2s), 1.30–1.17 (8H, m). ^{13}C NMR (75 MHz, $CDCl_3$) δ 155.9, 155.3, 154.4, 153.9, 140.6, 137.8, 137.7, 137.1, 137.0, 134.94, 134.91, 134.89, 134.83, 133.7, 133.6, 132.7, 132.1, 131.3, 131.2, 131.1, 131.0, 130.8, 130.4, 130.3, 128.2, 128.0, 127.8, 127.7, 126.3, 126.1, 118.9, 118.0, 115.5, 115.4, 115.35, 115.32, 113.4, 112.7, 111.2, 110.7, 83.8, 83.7, 70.5, 69.9, 68.5, 67.9, 39.4, 34.6, 34.5, 30.4, 30.3, 29.7, 29.4, 29.3, 29.2, 29.1, 29.08, 26.1, 26.02, 24.9, 22.6 (d, J = 49.8), 22.5 (J = 4.4).

2.5. Synthesis of MGN-B

Magnolol boronate (MGN-B) was prepared by reacting magnolol (MGN) in the presence of 2-(4-bromomethylphenyl)-4,4,5,5-tetramethyl-[1,3,2]-dioxaborolane and potassium carbonate in MeCN.

To a mixture of MGN (0.5 g, 1.92 mmol) and anhydrous potassium carbonate (0.34 g, 2.4 mmol) in MeCN (5 mL) was added 2-(4-bromomethylphenyl)-4,4,5,5-tetramethyl-[1,3,2]-dioxaborolane (0.57 g, 1.90 mmol). The mixture was stirred at reflux overnight. Then, ethyl acetate was added to the mixture as well as H_2O (20 mL). The organic layer was washed twice with H_2O and dried over Na_2SO_4. The solvent was removed under reduced pressure. Purification by flash chromatography (pentane/Et_2O 9/1 and 8/2) delivered the corresponding MGN-B (0.5 g, 55% yield). HRMS calculated for MGN-B $C_{31}H_{35}BO_4$ $[M+Na]^+$ 505.2526 returned 505.2528.

^{1}H NMR (400.13 MHz, $CDCl_3$) δ 7.71 (2H, d, J = 7.8), 7.21 (2H, d, J = 7.9), 7.13–7.04 (3H, m), 7.02 (1H, d, J = 1.6), 6.95 (1H, d, J = 8.2), 6.91 (1H, d, J = 8.2), 6.14 (1H, s), 6.01–5.87 (2H, m), 5.08–5.01 (6H, m), 3.33 (4H, d, J = 3.3), 1.29 (12H, s). ^{13}C NMR (75 MHz, $CDCl_3$) δ 153.2, 151.9, 139.2, 137.9, 137.3, 135.0, 133.4, 132.5, 132.2, 131.1, 129.3, 129.1, 128.1, 126.4, 126.1, 117.3, 115.9, 115.5, 114.5, 83.8, 71.8, 39.4, 24.8.

2.6. Synthesis of Mito-MGN-B

Mitochondria-targeted magnolol boronate (Mito-MGN-B) was prepared by reacting Mito-MGN in the presence of 2-(4-bromomethylphenyl)-4,4,5,5-tetramethyl-[1,3,2]-dioxaborolane and potassium carbonate in MeCN.

To a mixture of Mito-MGN (0.275 g, 0.37 mmol) and anhydrous potassium carbonate (0.076 g, 0.55 mmol) in MeCN (5 mL) was added 2-(4-bromomethylphenyl)-4,4,5,5-tetramethyl-[1,3,2]-dioxaborolane (0.14 g, 0.47 mmol). The mixture was stirred at reflux overnight. Then, CH_2Cl_2 was added to the reaction mixture as well as H_2O (20 mL). The organic layer was washed twice with H_2O and dried over Na_2SO_4. The solvent was

removed under reduced pressure. The residue was washed with Et_2O. Purification by flash chromatography (from CH_2Cl_2 to CH_2Cl_2/EtOH 95/05) delivered the corresponding Mito-MGN-B as a white solid (0.15 g, 42% yield). HRMS calculated for Mito-MGN-B ($C_{59}H_{69}BBrO_4P$ $[M]^+$ 883.5031 returned 883.5032).

^{31}P (400.13 MHz, $CDCl_3$) δ 24.32. ^1H NMR (400.13 MHz, $CDCl_3$) δ 7.85–7.64 (17H, m), 7.23–7.02 (6H, m), 6.87 (1H, d, *J* = 5.5), 6.85 (1H, d, *J* = 5.4), 6.01–5.89 (2H, m), 5.09–4.95 (6H, m), 3.81 (2H, t, *J* = 6.5), 3.75–3.66 (2H, m), 3.37–3.29 (4H, m), 1.55–1.43 (3H, m), 1.32–1.29 (12H, s), 1.25–1.21 (7H,m), 1.16–1.05 (6H, m). ^{13}C NMR (75 MHz, $CDCl_3$) δ 154.9, 154.4, 140.8, 137.85, 137.80, 134.95, 134.92, 134.62, 133.6, 133.5, 131.8, 131.79, 131.74, 131.4, 130.4, 130.3, 128.5, 128.2, 128.5, 127.9, 118.7, 117.9, 115.3, 112.8, 112.3, 83.7, 70.2, 68.5, 39.4, 30.4, 30.2, 29.3, 29.13, 29.10, 29.07, 28.9, 25.7, 24.9, 22.6 (d, *J* = 49.2), 22.5 (d, *J* = 4.4).

2.7. Synthesis of MAG-BET

Magnolol *ortho*-boronate (MAG-BET) was prepared by reacting MGN in the presence of 2-(2-bromomethylphenyl)-4,4,5,5-tetramethyl-[1,3,2]-dioxaborolane and potassium carbonate in MeCN.

To a mixture of MGN (0.5 g, 1.92 mmol) and anhydrous potassium carbonate (0.34 g, 2.4 mmol) in MeCN (5 mL) was added 2-(2-bromomethylphenyl)-4,4,5,5-tetramethyl-[1,3,2]-dioxaborolane (0.57 g, 1.90 mmol). The mixture was stirred at reflux for 32 h. Then, ethyl acetate was added to the mixture as well as H_2O (20 mL). The organic layer was washed twice with H_2O and dried over Na_2SO_4. The solvent was removed under reduced pressure. Purification by flash chromatography (pentane/Et_2O 9/1 and 8/2) delivered the corresponding MAG-BET (0.25 g, 27% yield). HRMS calculated for MAG-BET $C_{31}H_{35}BO_4$ $[M+Na]^+$ 505.2526 returned 505.2522.

^1H NMR (400.13 MHz, $CDCl_3$) δ 7.85 (1H, d, *J* = 7.3), 7.41–7.28 (3H, m), 7.19–7.14 (2H, m), 7.11–7.04 (3H, m), 6.92 (1H, d, *J* = 8.1), 6.46 (1H, s), 6.06–5.94 (2H, m), 5.41 (2H, s), 5.15–5.03 (4H, m), 3.41–3.37 (4H, m), 1.31 (12H, s). ^{13}C NMR (75 MHz, $CDCl_3$) δ 153.5, 152.2, 142.4, 137.9, 137.5, 136.2, 133.7, 132.5, 132.0, 131.3, 131.2, 129.1, 128.9, 127.8, 127.6, 127.1, 126.5, 117.6, 115.7, 115.4, 113.8, 83.9, 71.1, 39.5, 39.4, 24.8.

2.8. Calculated Values of the Octanol/Water Partition Coefficients

The calculated octanol/H_2O partition coefficients (logP) of boronate analogs were assessed using a quantitative structure–activity relationship analysis and rational drug design as a measure of molecular hydrophobicity (Figure 1). This method also uses a consensus model built using the ChemAxon software (San Diego, CA, USA) [47,48].

2.9. LC/MS Analysis

High-performance liquid chromatography (HPLC) analysis was performed using an Agilent 1200 apparatus equipped with ultraviolet–visible spectroscopy absorption and a mass spectrometry detector (single quadrupole).

In the studies on the reaction profile of $ONOO^-$ oxidation of Mito-HNK-B and derivatives, 2 µL of sample was injected into the HPLC system equipped with a C18 column (Phenomenex, Kinetex Evo, 100 × 2.1 mm, 1.7 µm) equilibrated with 5% MeCN containing 0.1% (*v*/*v*) formic acid. The compounds were separated by a linear increase in MeCN phase concentration from 5% to 100% over 8 min and until 15 min at 100% MeCN using a flow rate of 0.21 mL/min. The peak areas detected by monitoring the absorption at 260 nm were used for the quantitation.

2.10. Oxidation of Boronates Derivatives by $ONOO^-$, H_2O_2, and HOCl

The stock solutions of oxidants (HOCl and H_2O_2) were prepared freshly before each experiment; their concentrations were determined by spectrophotometry by reacting nitrite with H_2O_2, using the procedure described previously [15]. $ONOO^-$ was prepared according to the published procedure. Typically, $ONOO^-$ was synthesized in a reaction of 0.6 M nitrite with 0.7 M H_2O_2 at pH 13. Excess H_2O_2 was removed by passage through a column

of MnO_2 and the solution was frozen at −20 °C. The liquid over the frozen solid was collected and stored at −80 °C. Immediately prior to each experiment, the concentration of $ONOO^-$ was determined spectrally at 302 nm ($\varepsilon = 1.7 \times 103\ M^{-1}cm^{-1}$) after dilution in 0.1 M sodium hydroxide to ~10 mM concentration [49].

Stock solutions of HNK-B, HNK-B^2, and Mito-HNK-B were prepared in dimethyl sulfoxide at a 10 mM concentration and this solution was added directly to the buffer to obtain the desired concentration. HPLC analysis indicated that HNK-B, HNK-B^2, and Mito-HNK-B (pinacolate ester) undergo fast hydrolysis to the corresponding boronic acid formed upon dilution in the aqueous phosphate buffer. Thus, the boronic acid species were tested with the oxidants. When studying HNK-B and Mito-HNK-B oxidations by HOCl, stock solutions (10 mM) in MeCN were added to the phosphate buffer (100 mM, pH 7.4) to obtain a final concentration of the probe of 500 μM. Dimethyl sulfoxide solvent was avoided due to known rapid quenching of HOCl by dimethyl sulfoxide [50].

A study of the reactivity of HNK-B^2 in the presence of sodium hypochlorite (NaOCl) was not possible because its solubility is too low in MeCN and water.

3. Results

3.1. Hydrophobicity of Polyphenolic Boronates

Figure 1 lists the calculated partition coefficients for polyphenols (HNK, MGN, Mito-HNK, and Mito-MGN) and their boronate conjugates (HNK-B, HNK-B^2, $Mito_{10}$-HNK, $Mito_{10}$-HNK-B, MGN-B, MGN-B^2, $Mito_{10}$-MGN, $Mito_{10}$-MGN-B). Boronation increases the hydrophobicity of polyphenols. HNK-B^2 is significantly more hydrophobic than HNK.

3.2. Antiproliferative Effects of Polyphenolic Boronates in Glioblastoma, Melanoma, Pancreatic Cancer, and Lung Cancer Cell Lines

We compared the effects of polyphenols (MGN, HNK) and their boronate analogs (Mito-MGN-B and Mito-HNK-B) in the glioblastoma (U87MG), melanoma (UACC-62), pancreatic cancer (MiaPaCa-2), and lung cancer (A549) cell lines (Figures 2–5). Figure 2 shows the dose-dependent effects of HNK and HNK-B in glioblastoma (U87MG), pancreatic cancer (MiaPaCa-2), and lung cancer (A549) cells. In these cell lines, the antiproliferative effects of HNK and HNK-B were nearly the same. Figure 3 shows the dose-dependent effects of Mito-HNK and Mito-HNK-B in these cell lines, and the antiproliferative effects of Mito-HNK and Mito-HNK-B were nearly the same. As shown in Figure 4, glioblastoma cells were treated with Mito-MGN/Mito-MGN-B and MGN/MGN-B. Boronation increased the potency of MGN-B as compared with MGN. Mito-MGN-B was also slightly more potent than Mito-MGN (Figure 4). In both cases, triphenylphosphonium (TPP^+) conjugation (e.g., Mito-MGN and Mito-MGN-B) increased their antiproliferative potencies as compared with the parent compounds—MGN/MGN-B. Figure 5 shows the dose-dependent effects of MGN and MGN-B in decreasing the proliferation of melanoma (UACC-62) cells.

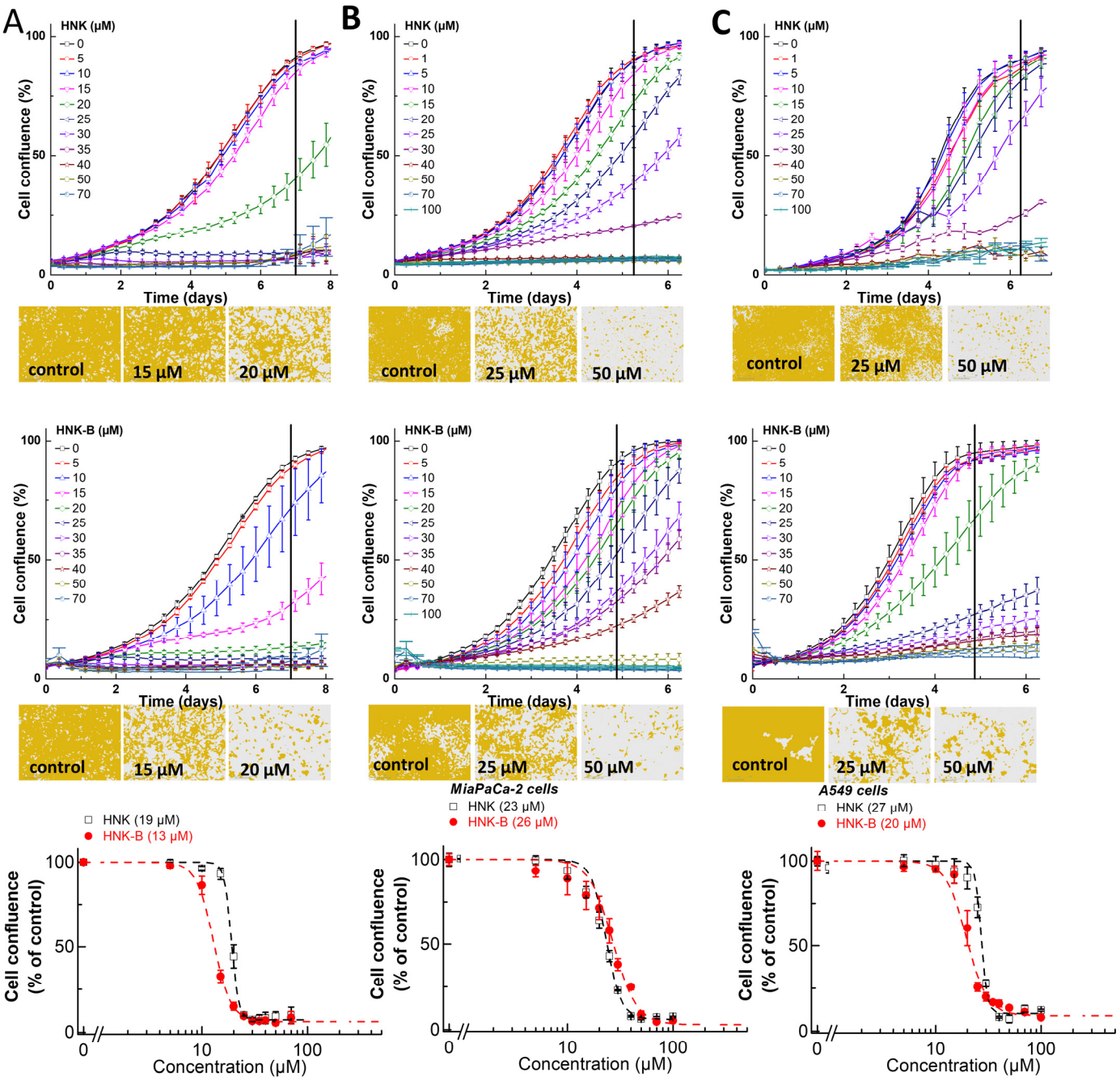

Figure 2. Effects of HNK and HNK-B on the proliferation of glioblastoma (U87MG), pancreatic cancer (MiaPaCa-2) cells, and lung cancer (A549) cells. The effects of HNK and HNK-B on the proliferation of U87MG (**A**), MiaPaCa-2 (**B**), or A549 (**C**) cells were monitored in the IncuCyte Live-Cell Analysis system. The IncuCyte analyzer provides real-time updates on cell confluence based on segmentation of high definition-phase contrast images. Representative cell images are shown as segmentation masks, illustrated in brown when control cells reached 90% confluence (vertical solid black line). The half maximal inhibitory concentration (IC_{50}) values for U87MG (**A**, **bottom**), MiaPaCa-2 (**B**, **bottom**), or A549 (**C**, **bottom**) cells were determined at the point at which control cells reached ~90% confluence (vertical solid black line). Relative cell confluence (control is taken as 100%) is plotted against concentration. Dashed lines represent the fitting curves used to determine the IC_{50} values as indicated. Data shown are the mean ± standard deviation (SD).

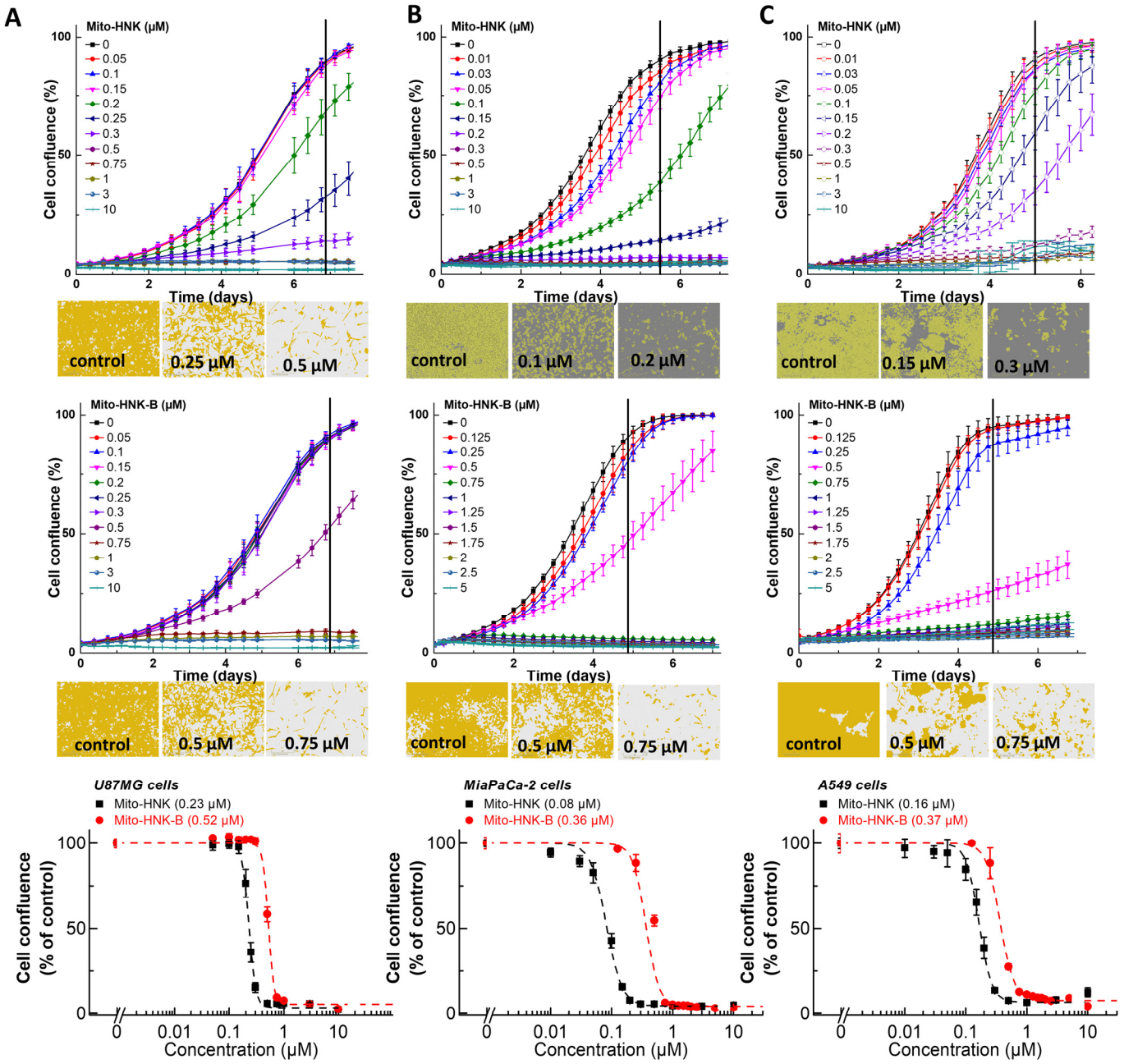

Figure 3. Effects of Mito-HNK and Mito-HNK-B on the proliferation of glioblastoma (U87MG), pancreatic cancer (MiaPaCa-2), and lung cancer (A549) cells. The effects of Mito-HNK and Mito-HNK-B on the proliferation of U87MG (**A**), MiaPaCa-2 (**B**), or A549 (**C**) cells were monitored in the IncuCyte Live-Cell Analysis system. The IncuCyte analyzer provides real-time updates on cell confluence based on segmentation of high definition-phase contrast images. Representative cell images are shown as segmentation masks, illustrated in brown when control cells reached 90% confluence (vertical solid black line). The IC_{50} values for U87MG (**A**, **bottom**), MiaPaCa-2 (**B**, **bottom**), or A549 (**C**, **bottom**) cells were determined at the point at which control cells reached ~90% confluence (vertical solid black line). Relative cell confluence (control is taken as 100%) is plotted against concentration. Dashed lines represent the fitting curves used to determine the IC_{50} values as indicated. Data shown are the mean ± SD.

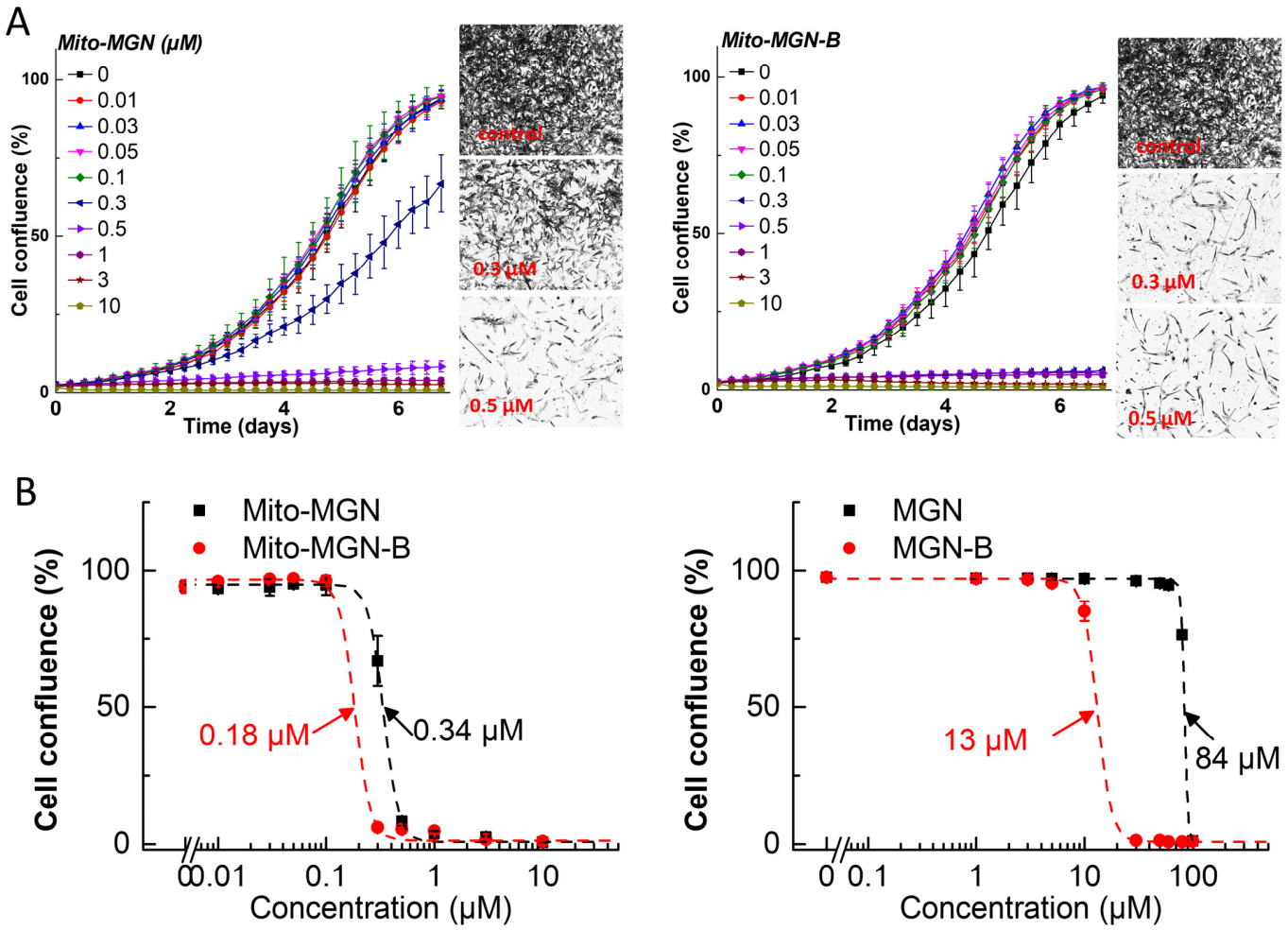

Figure 4. Effects of Mito-MGN, Mito-MGN-B, MGN, and MGN-B on the proliferation of glioblastoma cancer (U87MG) cells. The effects of Mito-MGN, Mito-MGN-B, MGN, and MGN-B on the proliferation of U87MG cells were monitored in the IncuCyte Live-Cell Analysis system. The IncuCyte analyzer provides real-time updates on cell confluence based on segmentation of high definition-phase contrast images. Representative cell images are shown as segmentation masks, illustrated in black when control cells reached 90% confluence. Full growth curves of Mito-MGN and Mito-MGN-B are shown in panel (**A**). The IC_{50} values were determined at the point at which control cells reached ~90% confluence. Relative cell confluence (control is taken as 100%) is plotted against concentration. Dashed lines represent the fitting curves used to determine the IC_{50} values as indicated for Mito-MGN and Mito-MGN-B in panel (**B**, **left**) for MGN and MGN-B in panel (**B**, **right**). Data shown are the mean ± SD.

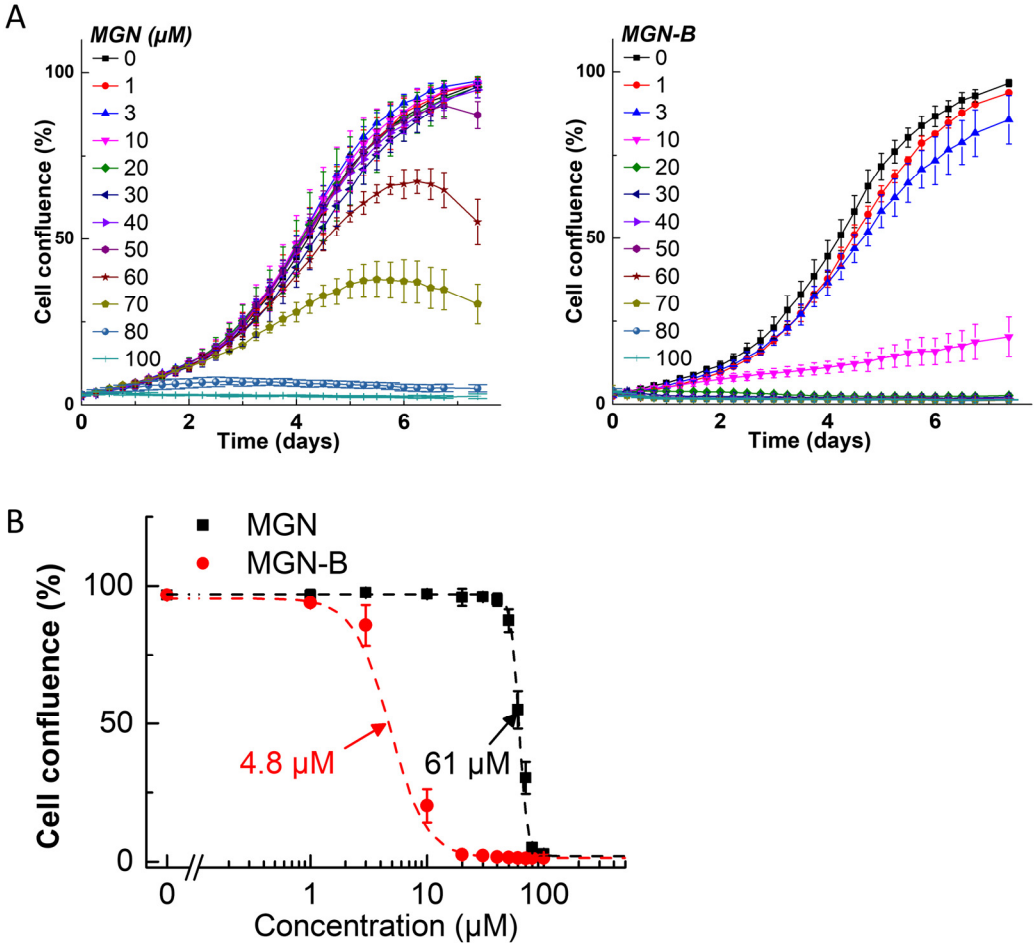

Figure 5. Effects of MGN and MGN-B on the proliferation of melanoma cancer (UACC-62) cells. The effects of MGN and MGN-B on the proliferation of UACC-62 cells were monitored in the IncuCyte Live-Cell Analysis system. The IncuCyte analyzer provides real-time updates on cell confluence based on segmentation of high definition-phase contrast images. Full growth curves of MGN and MGN-B are shown in panel (**A**). The IC_{50} values were determined at the point at which control cells reached ~90% confluence. Relative cell confluence (control is taken as 100%) is plotted against concentration. Dashed lines represent the fitting curves used to determine the IC_{50} values as indicated for MGN and MGN-B in panel (**B**). Data shown are the mean ± SD.

3.3. Reaction between Polyphenolic Boronates and Oxidants

Figures 6 and 7 show the HPLC traces and mass spectral parameters for HNK/HNK-B, Mito-HNK/Mito-HNK-B, and corresponding intermediates and products formed from the reaction with oxidants. In the presence of $ONOO^-$, both HNK-B and Mito-HNK-B were rapidly oxidized to HNK and Mito-HNK. In contrast, in the presence of H_2O_2, smaller conversion of HNK-B to HNK (60%) and Mito-HNK-B to Mito-HNK (37%) was observed. However, at higher concentrations of H_2O_2, this conversion was increased. These results are consistent with our original finding that $ONOO^-$ reacts with boronates considerably faster than H_2O_2 [51]. Nitrated HNK and Mito-HNK were likely formed in minor quantities. HPLC results also show the formation of the hydroxy intermediate that triggers the self-immolative pathway (see Discussion, Figure 8).

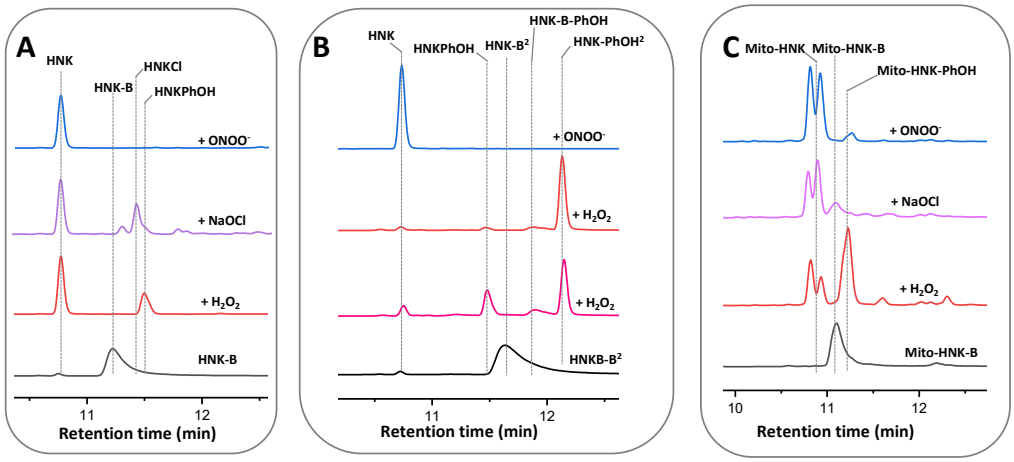

Figure 6. HPLC traces of the reaction between oxidants and HNK derivatives. (**A**) Reaction of HNK-B (500 μM) in the presence of H_2O_2, NaOCl, and $ONOO^-$ (500 μM). (**B**) Reaction of HNK-B^2 (500 μM) in the presence of H_2O_2 (500 μM and 2 mM) and $ONOO^-$ (500 μM). (**C**) Reaction of Mito-HNK-B (500 μM) in the presence of H_2O_2, NaOCl, and $ONOO^-$ (500 μM). All samples were incubated at room temperature in aqueous solution containing phosphate buffer (0.1 M, pH 7.4) and DTPA (10 μM). Absorption traces recorded using UV absorption detection at 260 nm.

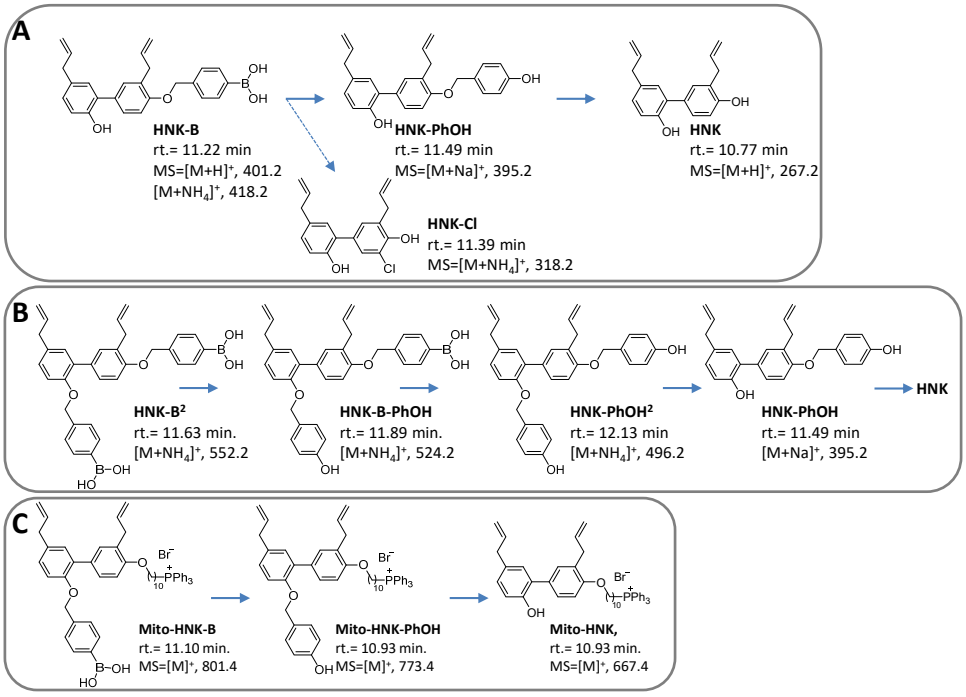

Figure 7. Structures, mass spectral parameters, and retention times of reactants, intermediates, and products formed from the reaction between oxidants and HNK derivatives. (**A**) Products formed from the reaction of HNK-B with oxidants. (**B**) As in (**A**) but in the presence of HNK-B^2. (**C**) As in (**A**) but in the presence of Mito-HNK-B.

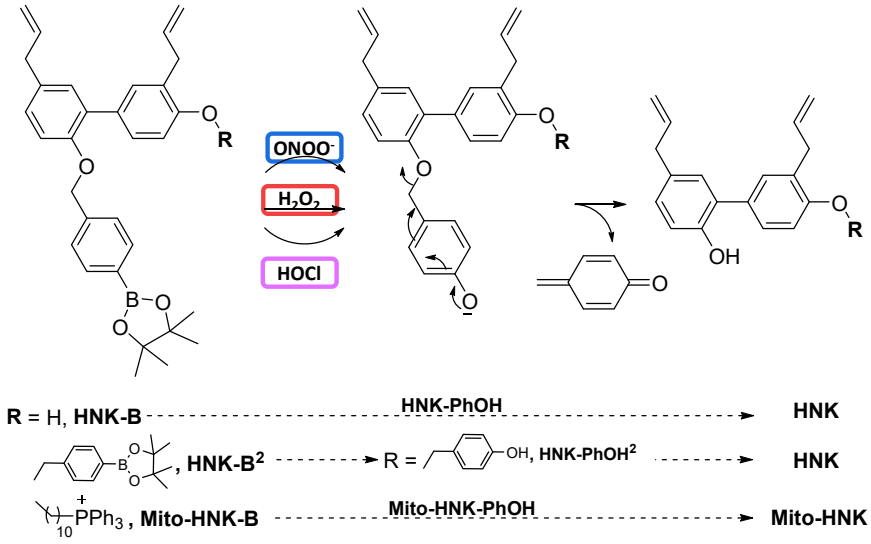

Figure 8. Oxidant-induced transformation of polyphenolic boronates to corresponding phenols.

4. Discussion

4.1. Oxidative Cleavage of Polyphenolic Boronates and TPP⁺-Conjugated Polyphenolic Boronates

The polyphenolic boronate compounds consist of an arylboronic ester head group and a quinone methide group linked via a carbamate group to the parent polyphenolic compound (e.g., HNK or Mito-HNK). In the presence of oxidants such as H_2O_2, HOCl, and $ONOO^-$, boronates are oxidized through insertion of an oxygen atom into the carbon–boron bond, forming the corresponding phenol intermediate. The phenoxide ion eliminates the quinone methide, releasing the polyphenolic compound via a decomposition process known as self-immolation (Figure 8). As shown in our previous publications [13,25,26], $ONOO^-$ reacts with boronates about one million times faster than H_2O_2 and one thousand times faster than HOCl. Phenols are the major product. Whereas the H_2O_2/boronate reaction is catalase-sensitive, the $ONOO^-$/boronate reaction is catalase-insensitive. Peroxy-caged luciferin (PCL-1) is oxidized by H_2O_2, HOCl, and $ONOO^-$ to luciferin as a major product through a self-immolation mechanism [15,20,27]. In an in vivo setting, PCL-1 has been used in luciferase-transfected mice xenografts to monitor oxidant formation through measurement of bioluminescence and in PET using a boronate-based positron emitting probe [16,20–22].

4.2. Antitumor Activity of MTDs: Activation of Immune Cells

We showed that mitochondria-targeted atovaquone (Mito-ATO) targets both granulocytic-myeloid-derived suppressor cells (G-MDSCs) and regulatory T cells (T_{regs}) in the TME, resulting in significant decreases of both G-MDSCs and T_{regs} as determined by flow cytometry analysis [45]. Intratumoral injection of Mito-ATO into primary tumors in a spontaneous tumor model triggered potent T cell immune responses locally and in distant tumor sites. Single-cell RNA sequencing revealed that Mito-ATO inhibits the expression of genes for OXPHOS and glycolysis in G-MDSCs and T_{regs} and facilitates the infiltration of $CD4^+$ T cells in the tumor microenvironment [52]. Other studies also revealed the immuno-modulatory and tumor-preventing effects of MTDs [53,54].

4.3. Oxidants in the Tumor Microenvironment: Potential Inhibition by Polyphenolic Boronates

The TME changes dynamically. The TME consists of tumor cells, cancer-associated macrophages, lymphocytes, neutrophils, cancer-associated fibroblasts, endothelial cells, and vascular pericytes. The extracellular matrix in the TME consist of protein and polysaccharides. The dynamic interaction or the lack thereof between the tumor cells and the many cells and components in the TME regulates metabolism. MDSCs generate reactive oxy-

gen and nitrogen species in the TME via activation of nicotinamide adenine dinucleotide phosphate oxidase (NOX) and inducible nitric oxide synthase (iNOS) [55].

We have previously reported the anti-inflammatory effects of MTDs in Mito-Park mice [56,57]. MTDs such as Mito-apocynin decreased the expression of iNOS and NOX2, resulting in decreased oxidative and nitrative damage in neuronal cells. In another study, administration of an MTD (i.e., mitochondria-targeted carboxy-proxyl [Mito-CP]) inhibited cisplatin-induced renal toxicity by inhibiting pro-inflammatory mediators (iNOS in macrophages) in the kidney [58]. Mitochondria-targeted compounds inhibit oxidants generated from NOX2 [56,59]. Inhibition of NOX4 (which presumably generates only H_2O_2) potentiates cancer immunotherapy [60,61]. Recent clinical trials using iNOS inhibitors in breast cancer patients who were resistant to other forms of cancer therapies showed tumor shrinkage and enhanced patient survival [62]. Inhibition of nitric oxide generated in the TME from tumor-associated macrophages decreased inflammatory mediators in the TME and enhanced killing of cancer cells by T cells.

In the present study, the reaction between polyphenolic boronates and reactive oxygen/nitrogen species released the parent polyphenolic compounds in situ. When MTD is released, it may inhibit iNOS and nitric oxide generation in the TME, thus decreasing inflammation. Figure 9 shows the antioxidant potentials of Mito-HNK-B/Mito-MGN-B and HNK-B/MGN-B in the TME, especially the direct and nearly stoichiometric scavenging of $ONOO^-$. The compound 3-(aminocarbonyl) furoxan-4-yl) methyl salicylate (AT38) was used to enhance the efficacy of immunotherapy in pancreatic cancer [40]. AT38 inhibited the expression of arginase-1 and NOS-2 (or iNOS) in myeloid cells in the TME [41]. AT38 mitigated chemokine nitration, promoting intra-tumoral infiltration of T cells. It is not clear if AT38 had any effect on NOX2 expression or on formation of superoxides and H_2O_2. Boronate-based drugs are likely to be more potent scavengers of $ONOO^-$ (and HOCl), even in the presence of cellular reductants such as glutathione. Detection of the minor nitrated or chlorinated product from polyphenolic boronates can serve as a very reliable and diagnostic marker product of $ONOO^-$ or HOCl generated in the TME. Preliminary results obtained from our laboratory indicate that Mito-HNK inhibits oxidant formation from NOX2 (Zielonka J and Kalyanaraman B, unpublished data). At present, the inhibitory effects of Mito-HNK or Mito-MGN or their boronate analogs on iNOS and NOX2 expression in cells are not known.

4.4. Mitochondria-Targeted Boronates as Radiosensitizers

Boronated agents (e.g., boronophenylalanine) are used to enhance the therapeutic ratio in neutron treatment of cancers. This BNCT modality involves selective delivery of boron-10 to tumors followed by irradiation with neutrons. During this process, lithium-7 and an alpha particle that are generated destroy the tumor tissues [1–5]. BNCT has been used clinically to treat cancers, including glioblastoma multiforme, head and neck cancers, lung cancer, and breast cancer. A critical requirement for enhanced therapeutic success is selective localization of boron-containing compounds in tumor tissues. Mitochondria-targeted boronates (Mito-HNK-B and Mito-MGN-B) that are selectively sequestered in tumor mitochondria could be more effective in capturing neutrons in mitochondria of tumors and enhance tumor killing.

Inhibition of mitochondrial respiration could alleviate tumor and TME hypoxia and act as radiation sensitizers. Mitochondria-targeted metformin and X-radiation sensitized the killing of pancreatic cancer cells [46,63]. Clinical trials are ongoing with atovaquone and radiation therapy [64]. Tumor hypoxia inhibits the efficacy of radiation and immunotherapies in cancer. Targeting mitochondrial metabolism in non-small cell lung cancer patients was reported to modify both the tumor and TME through a decrease in hypoxia and hypoxic gene expression [65,66]. Mitochondria-targeted drugs decrease tumor hypoxia (or increase tumor oxygenation) by inhibiting mitochondrial respiration in tumors. Blood–brain-barrier-permeable aromatic boronates were effective in treating brain tumors using neutron capture therapy [1,6]. Although it is not known whether mitochondria-targeted

polyphenolic boronates (Mito-MGN-B and Mito-HNK-B) are blood–brain-barrier permeable, Mito-HNK inhibited metastasis of lung tumors to the brain in mice xenografts and showed blood–brain-barrier permeability [43].

4.5. Mitochondria Metabolism and Racial Disparity in Cancer

Recent publications suggest that race and ethnicity are factors that affect mitochondrial metabolism in cancer cells, and that mitochondrial metabolism in white cancer patients is considerably different than in patients from other racial and ethnic groups [67–70]. Studies have revealed distinct differences in the TME in Black cancer patients. In Black patients with bladder cancer, mitochondrial metabolism is considerably higher [71]. Although more studies are needed to fully substantiate this trend, the differential metabolism provides a compelling rationale for testing mitochondria-targeted drugs in Black patients with bladder cancer.

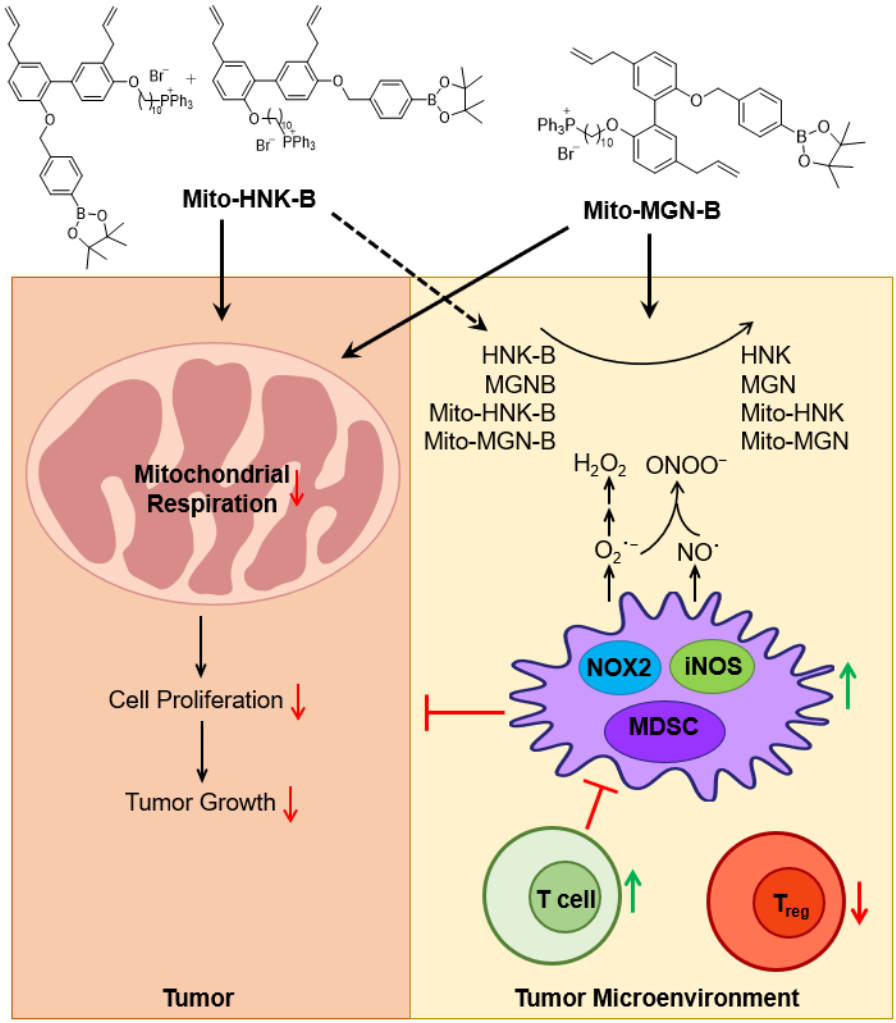

Figure 9. The proposed antiproliferative and antioxidant potential of polyphenolic boronates in tumor mitochondria and the TME. One of the mechanisms of immunosuppression in the TME is myeloid cell-induced generation of reactive oxygen species and reactive nitrogen species (H_2O_2 and $ONOO^-$). Boronates can remove reactive oxygen species and reactive nitrogen species and activate T cells in addition to generating polyphenols and mitochondria-targeted polyphenols in situ in the tumor microenvironment. This figure was modified from [68], with permission from John Wiley and Sons.

The existence of racial and ethnic disparities has been identified in the breast cancer microenvironment [72–74]. The TME of Black cancer patients with breast cancer exhibits in-

creased level pro-tumorigenic factors (e.g., macrophages, T_{regs}, exhausted T cells) compared with white counterparts [67,68,72,75]. Upregulation of OXPHOS genes was detected in tumor samples isolated from Black cancer patients [76]. Tumors obtained from Black cancer patients have more mitochondria and PGC-1α (proliferation-activated receptor gamma coactivator 1-alpha) [69]. Identification of biomarkers (e.g., hypoxia-induced genes) in these patients may provide additional insights [65]. Black cancer patients were reported to exhibit a higher level of pro-inflammatory cytokines [76]. Clinical trials targeting mitochondrial metabolism in cancer should include Black patients and patients from diverse racial and ethnic backgrounds. Presently, metformin is used as the sole drug of choice to test the mechanistic role of mitochondria in cancer disparity studies [67,77]. Metformin is one of the most prescribed drugs for treating diabetes. Despite increased safety, its bioavailability is poor. Clinical trials revealed that Black cancer patients respond better to mitochondrial OXPHOS inhibitors (e.g., metformin) than white cancer patients [67,77]. The present study opens the possibility of testing a new class of mitochondria-targeted drugs that target both the tumor mitochondria and TME to treat Black cancer patients.

5. Conclusions

The development of drugs that target both the tumor mitochondria and the TME would be a value-adding therapeutic advancement [78–82]. Higher expression of OXPHOS in triple-negative breast cancer patients who received neoadjuvant chemotherapy was associated with worse treatment outcome [83]. In this study, we developed a novel class of mitochondria-targeted polyphenolic boronates that inhibit tumor cell proliferation and scavenge oxidants such as H_2O_2, HOCl, and $ONOO^-$ that are generated in the immunosuppressive TME. During this reaction, immunoactive parent polyphenols are regenerated. Specific polyphenols include HNK and MGN, which are active components of magnolia plant extract. Borono-L-phenylalanine was used to treat brain cancer in humans, so it is likely that polyphenolic boronates and the mitochondria-targeted boronate analogs are nontoxic and have high clinical and translational potential. We hope that the redox-based mitochondria-targeted polyphenolic boronates will be tested in the appropriate mice models (e.g., KPC mice) to assess their ability to inhibit reactive oxygen species/reactive nitrogen species-mediated nitration in the TME.

Author Contributions: Conceptualization, G.C., H.K., M.H. and B.K.; methodology, G.C. and M.H.; software, G.C. and M.H.; validation, G.C., M.H. and B.K.; formal analysis, G.C., M.H. and B.K.; investigation, G.C., M.H. and B.K.; resources, M.H. and B.K.; data curation, G.C. and M.H.; writing—original draft, M.H. and B.K.; writing—review and editing, G.C., M.H. and B.K.; visualization, G.C. and M.H.; supervision, B.K.; project administration, G.C., M.H. and B.K.; funding acquisition, M.H. and B.K. All authors have read and agreed to the published version of the manuscript.

Funding: The project upon which this publication is based was performed pursuant to an agreement with The Methodist Hospital Research Institute, which in turn was supported by Grant Number R01CA208648 from the National Institutes of Health. Additionally, this project was supported in part by the International Research Project $SuperO_2$ from CNRS, France.

Data Availability Statement: Not applicable.

Acknowledgments: Thanks to Lydia Washechek for preparing and proofreading the manuscript.

Conflicts of Interest: B.K. and M.H. are co-inventors of US patent no. 10,836,782/European Patent No. 3307254, "Mito-honokiol compounds and methods of synthesis and use thereof," and B.K., G.C. and M.H. are co-inventors of US patent no. 11,083,739, "Mito-magnolol compounds and methods of synthesis and use thereof," for use of Mito-HNK and Mito-MGN, respectively, in the treatment of cancer. The funders had no role in the design of the study; in the collection, analyses, or interpretation of data; in the writing of the manuscript; or in the decision to publish the results.

Abbreviations

AT38	3-(aminocarbonyl) furoxan-4-yl) methyl salicylate
BNC	boron neutron capture therapy
$CDCl_3$	deuterated chloroform
CH_2Cl_2	dichloromethane
Et_2O	diethyl ether
EtOH	ethanol
G-MDSCs	granulocytic-myeloid-derived suppressor cells
H_2O	water
H_2O_2	hydrogen peroxide
HNK	honokiol
HNK-B	honokiol boronate
HNK-B^2	honokiol diboronate
HOCl	hypochlorous acid
HPLC	high-performance liquid chromatography
HRMS	high-resolution mass spectrometry
IC_{50}	half maximal inhibitory concentration
iNOS	inducible nitric oxide synthase
logP	octanol/H_2O partition coefficients
MAG-BET	magnolol *ortho*-boronate
MeCN	acetonitrile
MGN	magnolol
MGN-B	magnolol boronate
Mito	mitochondria-targeted
Mito-ATO	mitochondria-targeted atovaquone
Mito-CP	mitochondria-targeted carboxy-proxyl
Mito-HNK	mitochondria-targeted honokiol
Mito-HNK-B	mitochondria-targeted honokiol boronate
Mito-MGN	mitochondria-targeted magnolol
Mito-MGN-B	mitochondria-targeted magnolol boronate
MTD	mitochondria-targeted drug
NOX	nicotinamide adenine dinucleotide phosphate oxidase
Na_2SO_4	sodium sulfate
NaOCl	sodium hypochlorite
NMR	nuclear magnetic resonance
$ONOO^-$	peroxynitrite
OXPHOS	oxidative phosphorylation
PET	positron-emission tomography
SD	standard deviation
T_{regs}	regulatory T cells
TPP^+	triphenylphosphonium
TLC	thin layer chromatography
TME	tumor microenvironment
δ	chemical shifts

Appendix A

^{1}H NMR (400.13 MHz, $CDCl_3$)

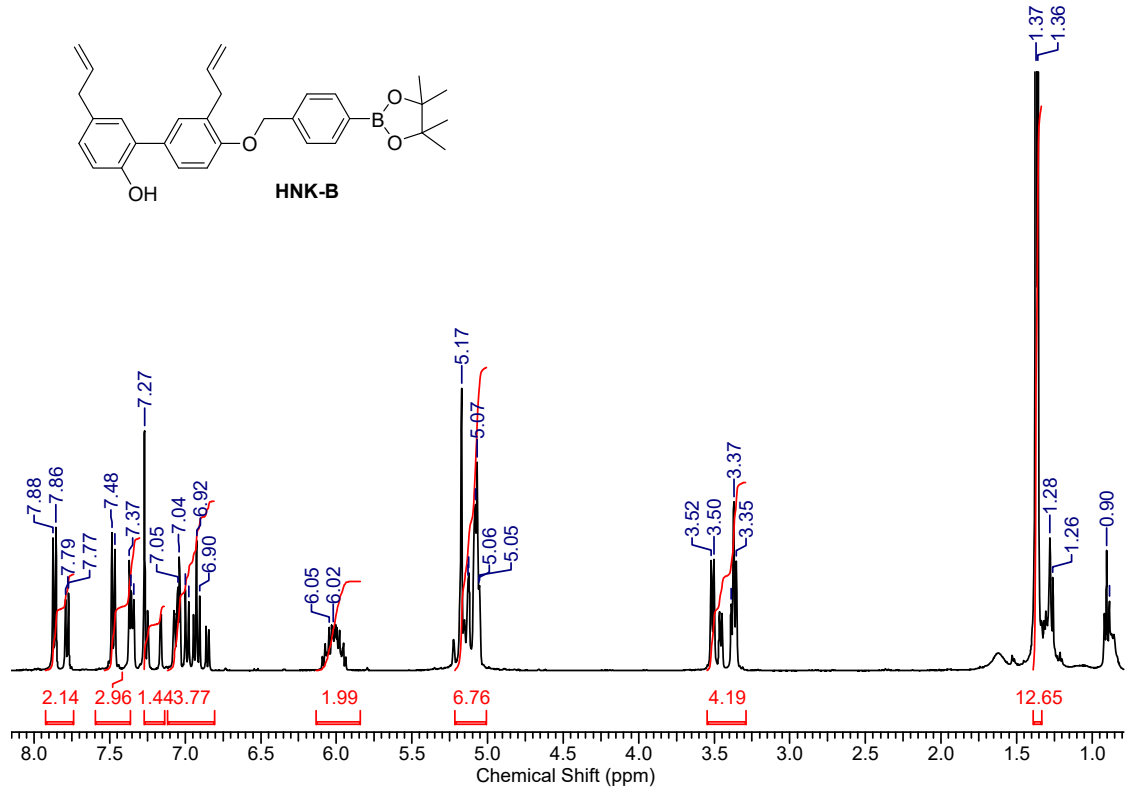

^{13}C (75 MHz, $CDCl_3$)

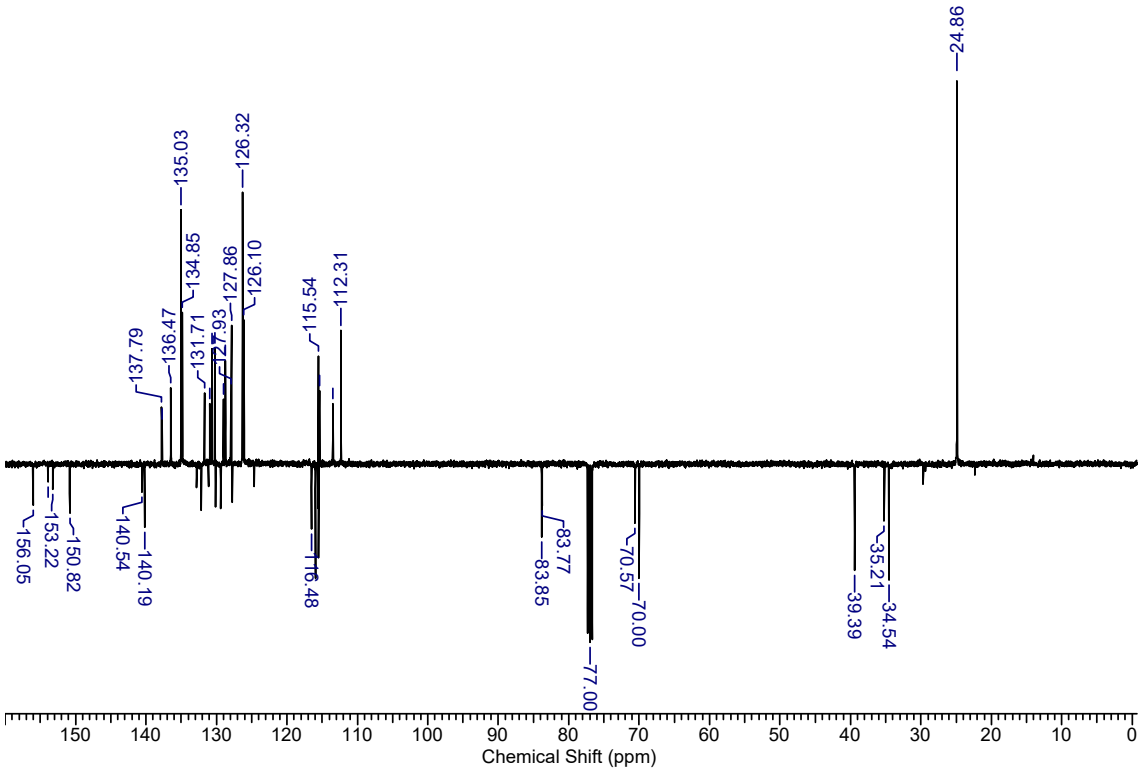

Figure A1. NMR Spectra of HNK-B.

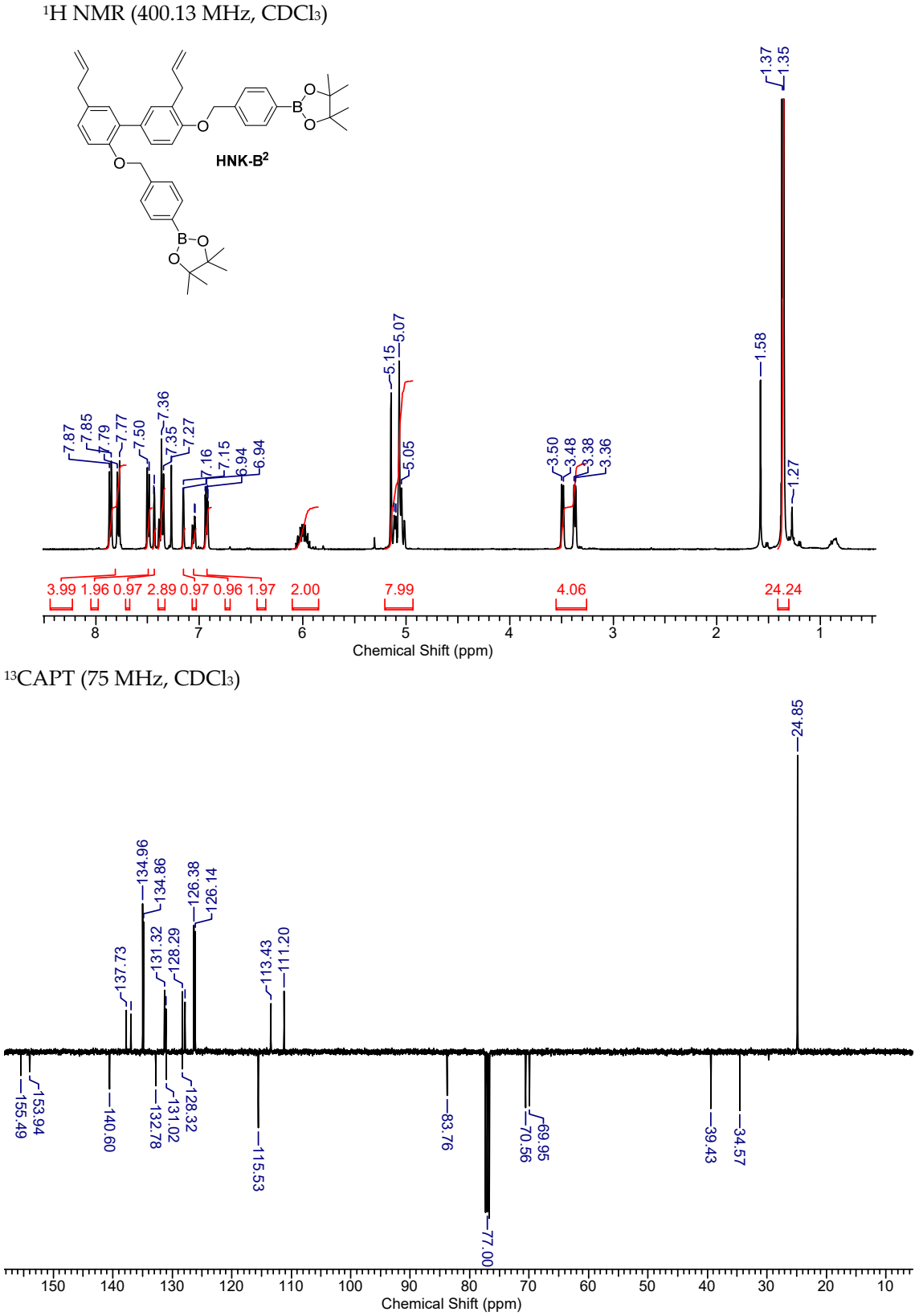

Figure A2. NMR Spectra of HNK-B2.

^{31}P (400.13 MHz, $CDCl_3$)

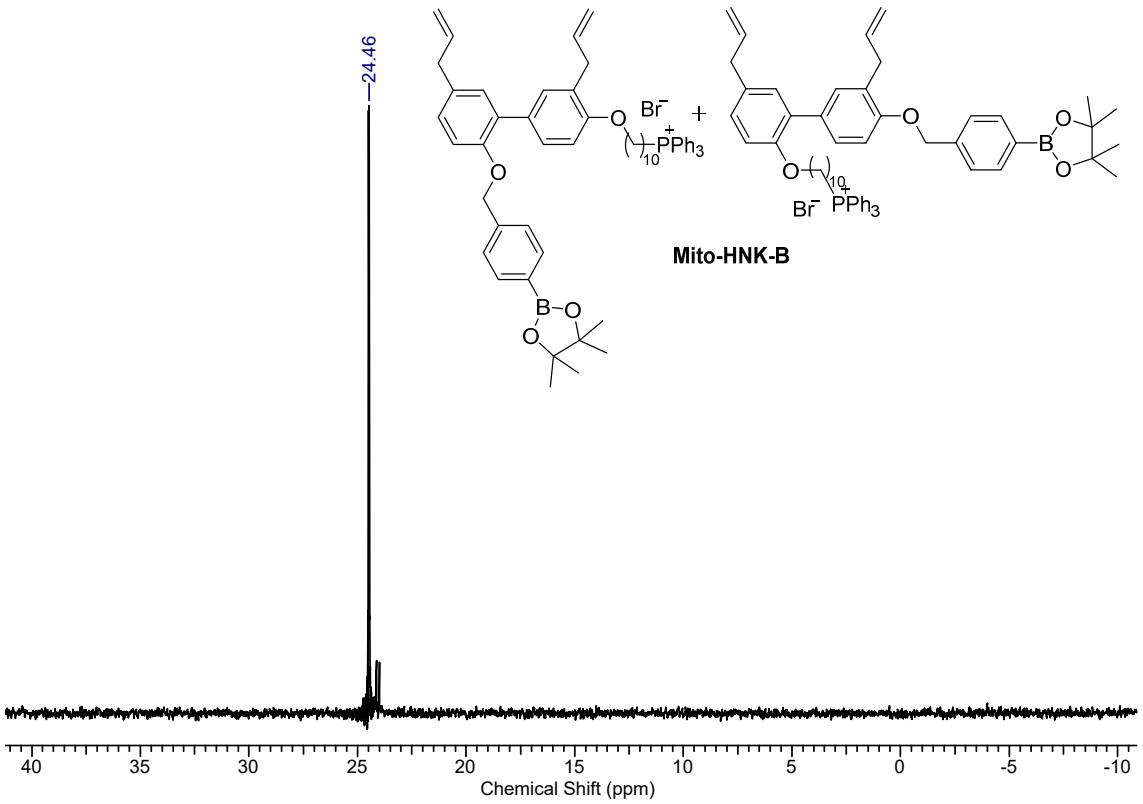

Figure A3. NMR Spectra of Mito-HNK-B.

^{1}H NMR (400.13 MHz, $CDCl_3$)

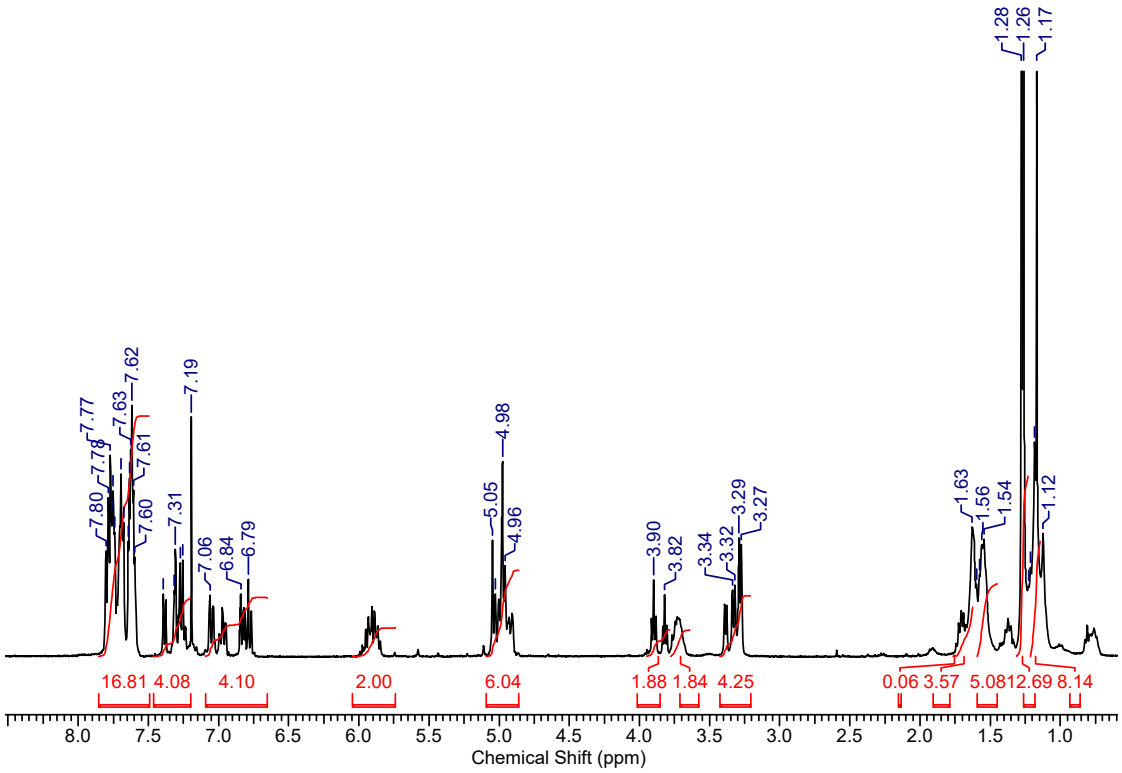

Figure A4. *Cont.*

^{13}C (75 MHz, $CDCl_3$)

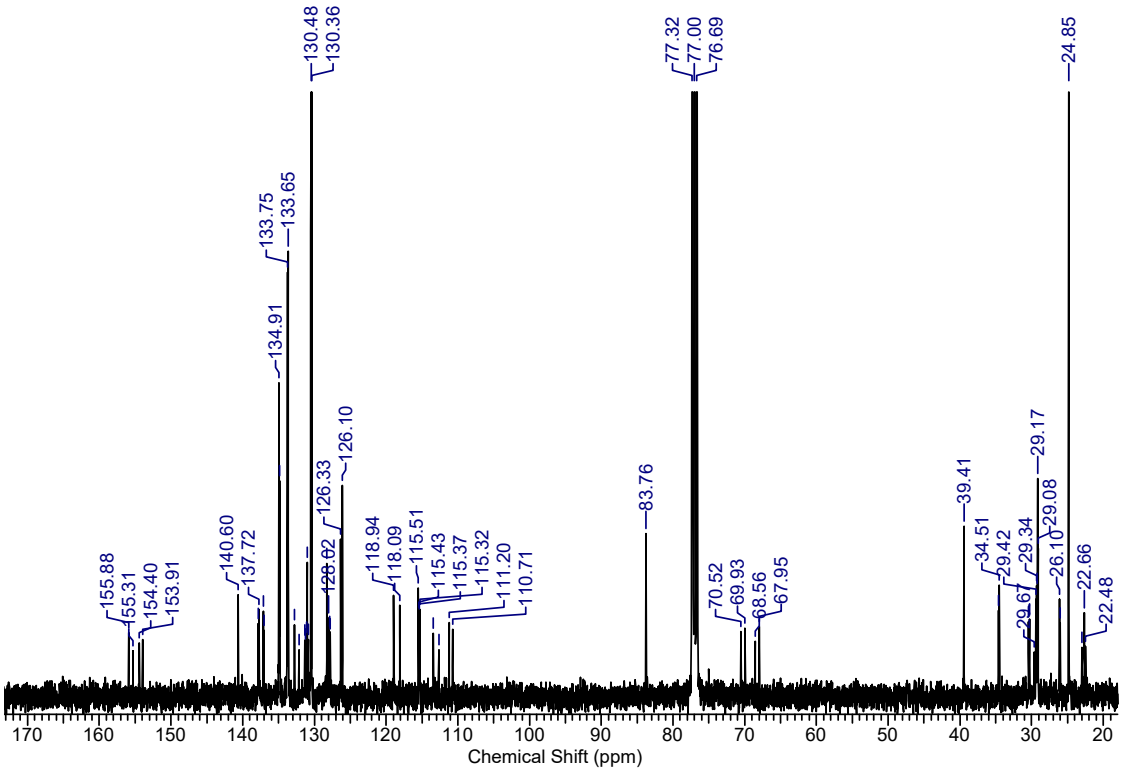

Figure A4. NMR spectra of Mito-HNK-B.

^{1}H NMR (400.13 MHz, $CDCl_3$)

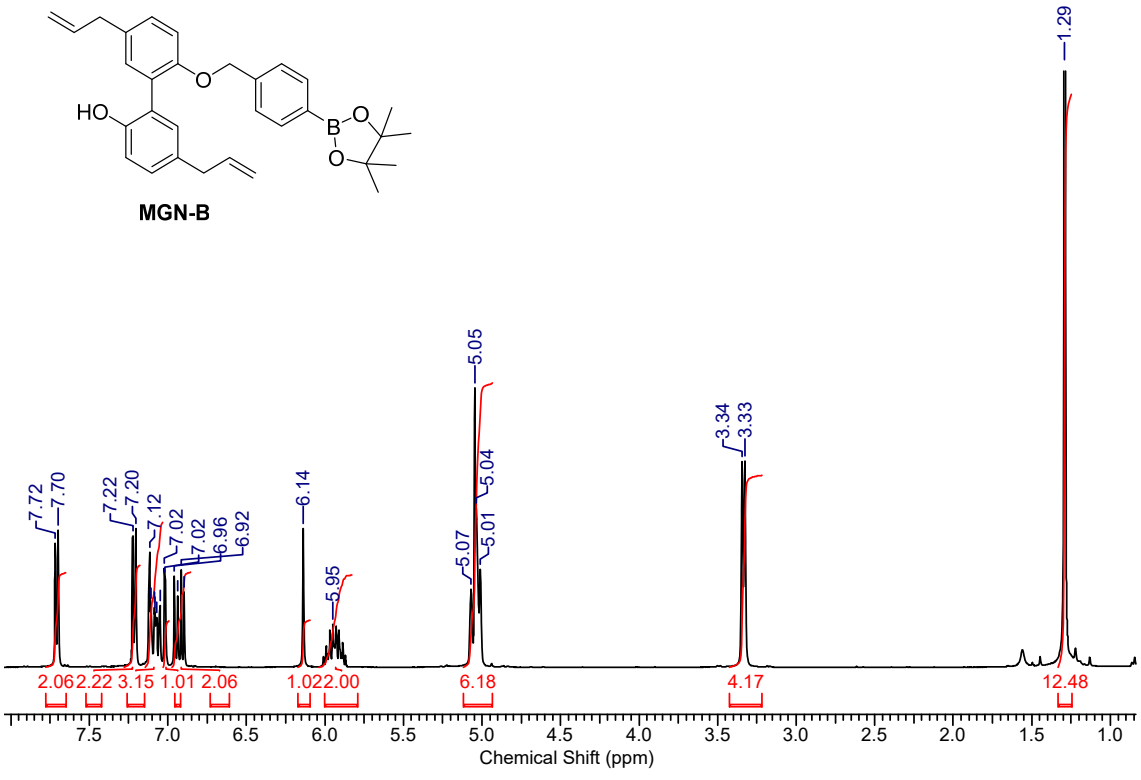

Figure A5. *Cont.*

^{13}C (75 MHz, $CDCl_3$)

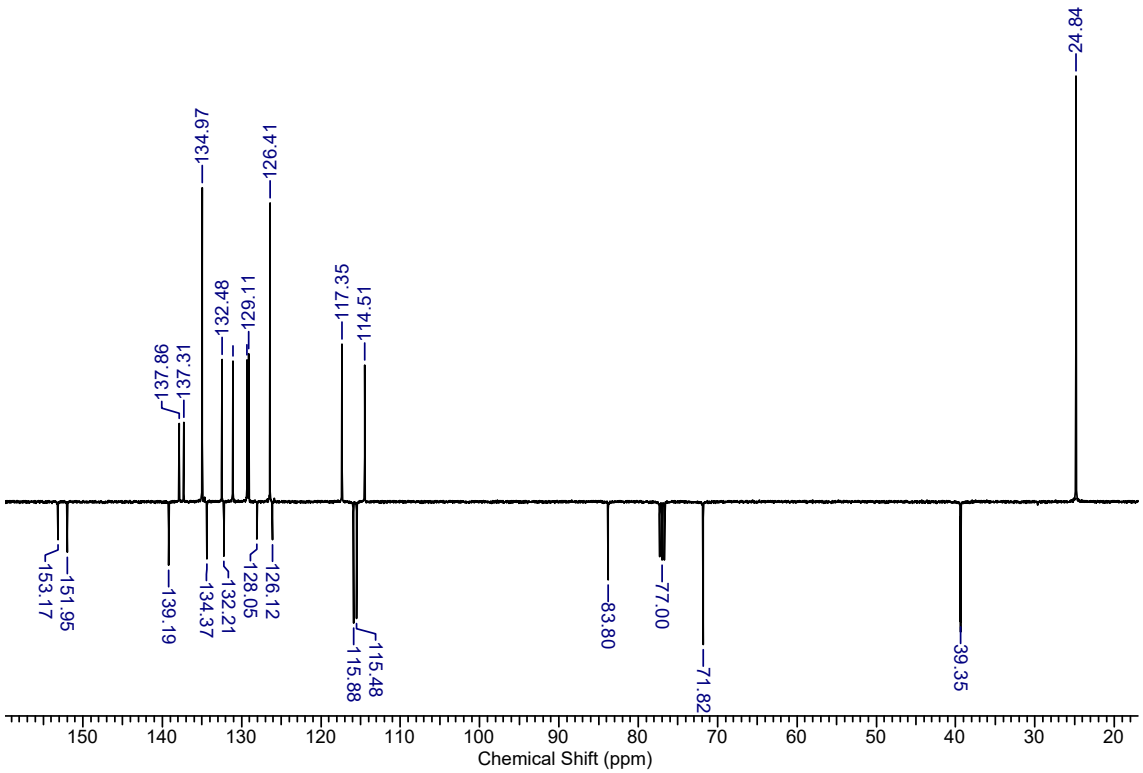

Figure A5. NMR Spectra of MGN-B.

^{31}P (400.13 MHz, $CDCl_3$)

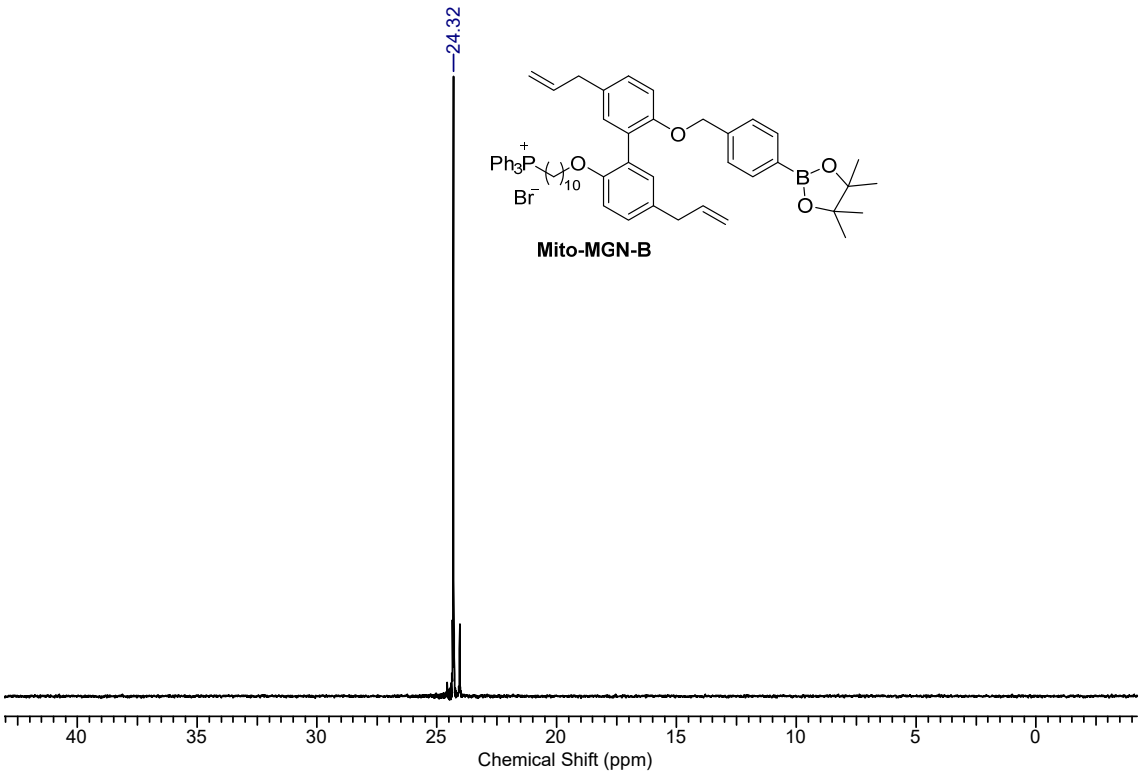

Figure A6. *Cont.*

^{1}H NMR (400.13 MHz, $CDCl_3$)

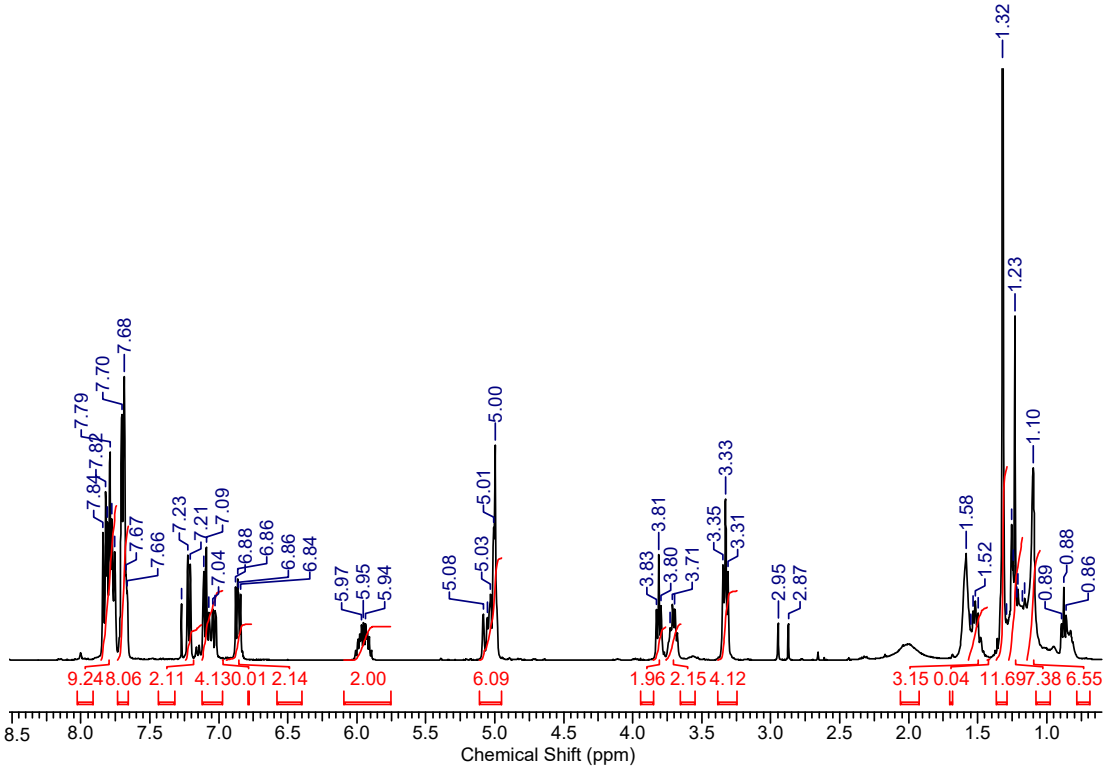

^{13}C (75 MHz, $CDCl_3$)

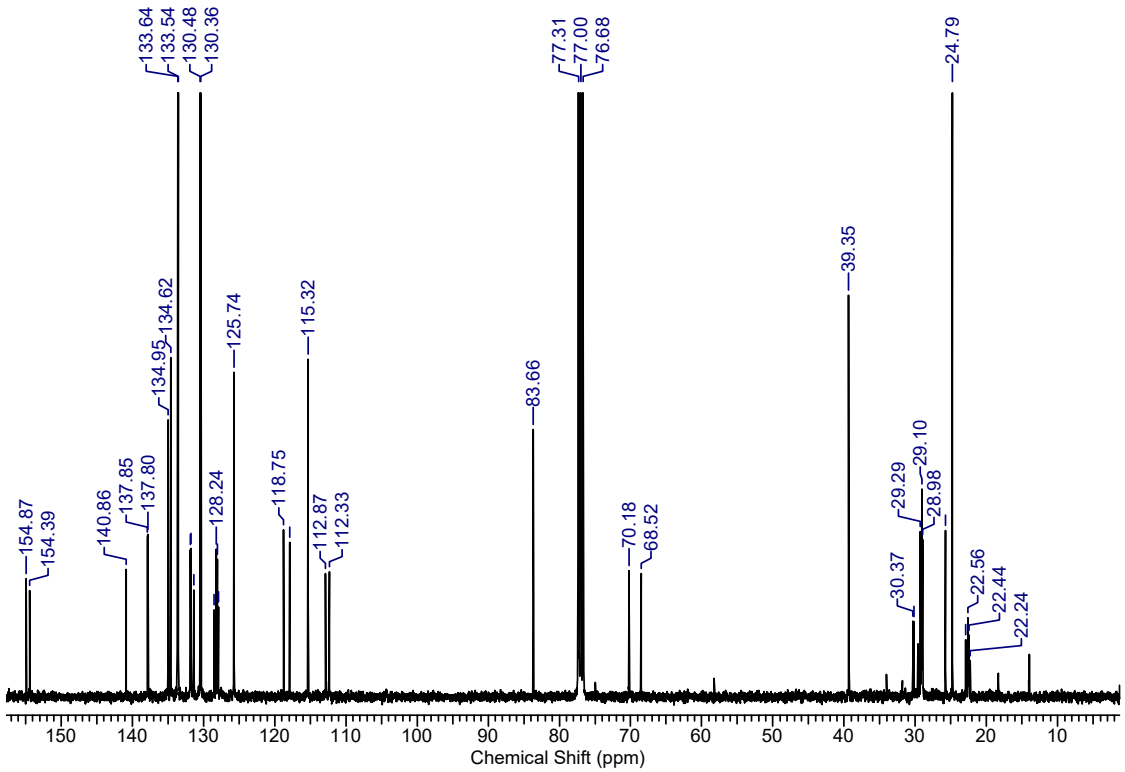

Figure A6. NMR Spectra of Mito-MGN-B.

^{1}H NMR (400.13 MHz, $CDCl_3$)

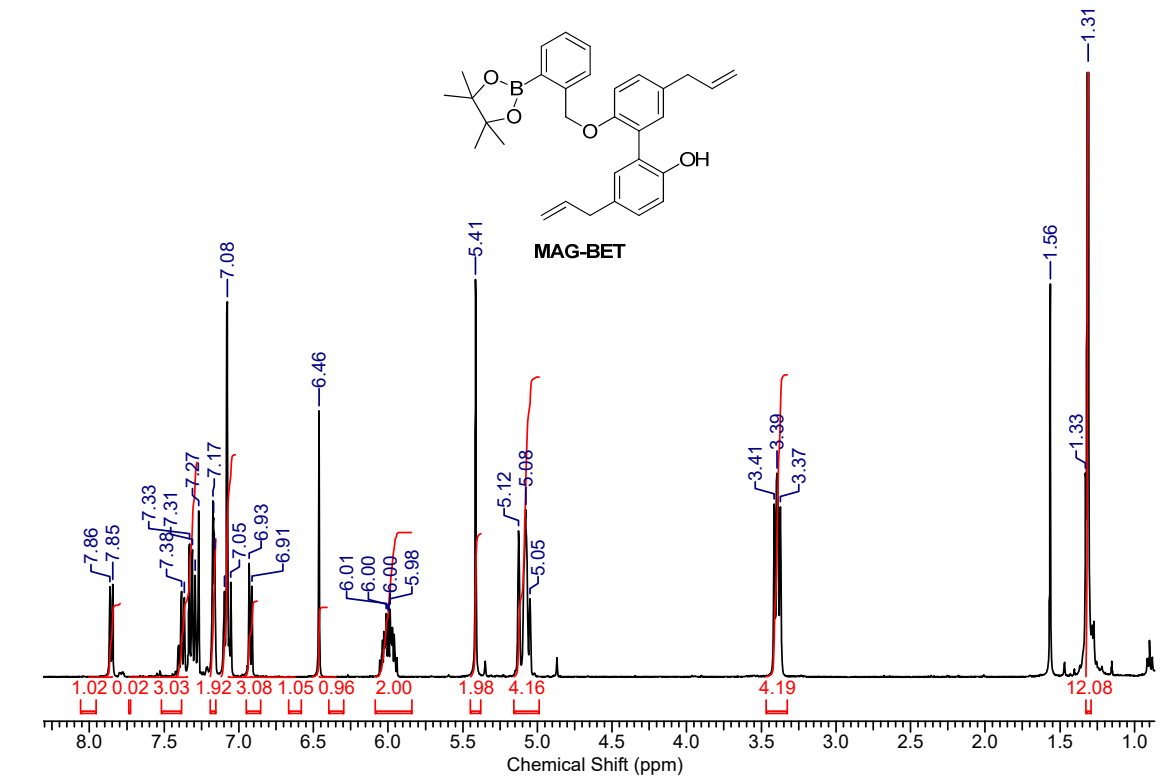

^{13}C (75 MHz, $CDCl_3$)

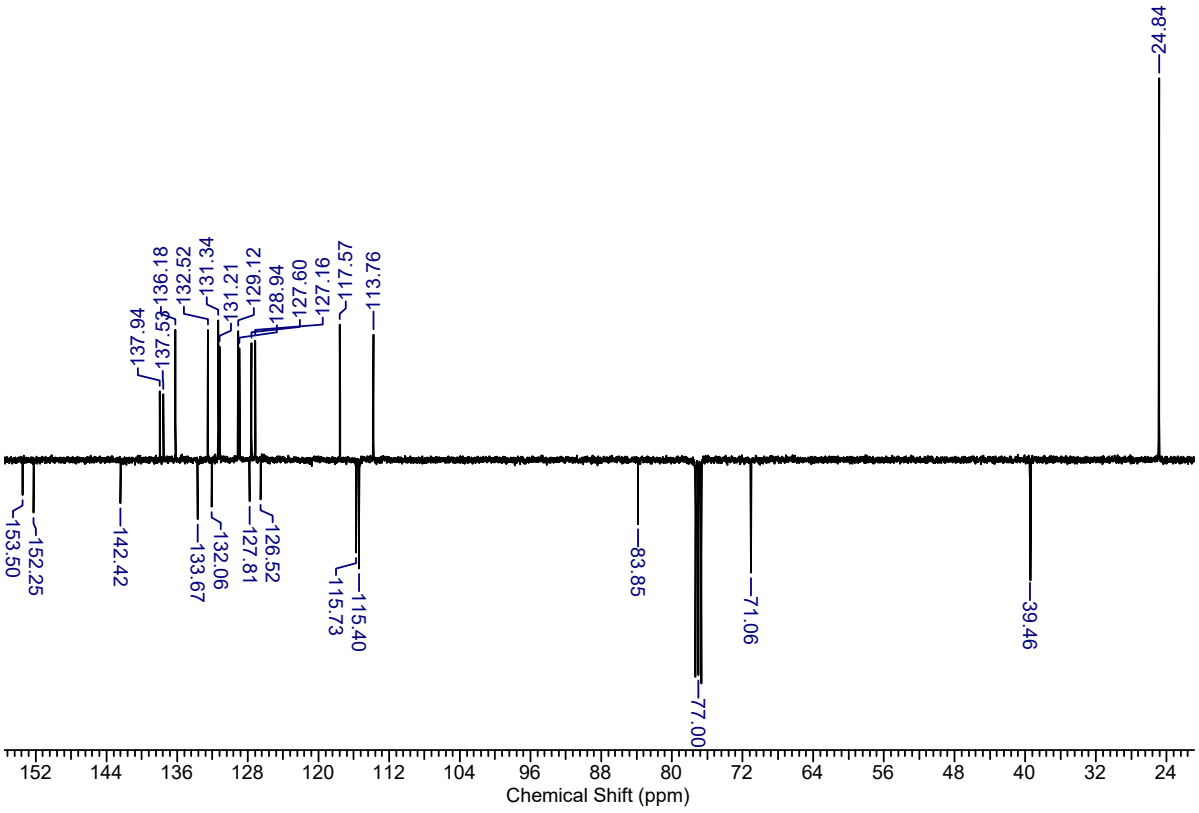

Figure A7. NMR Spectra of MAG-BET.

References

1. Malouff, T.D.; Seneviratne, D.S.; Ebner, D.K.; Stross, W.C.; Waddle, M.R.; Trifiletti, D.M.; Krishnan, S. Boron Neutron Capture Therapy: A Review of Clinical Applications. *Front. Oncol.* **2021**, *11*, 601820. [CrossRef] [PubMed]
2. Luderer, M. Development of Novel Tumor-Targeted Compounds for Boron Neutron Capture Therapy. Ph.D. Thesis, Washington University, St. Louis, MO, USA, 2019.
3. Chen, Y.W.; Chou, F.I.; Huang, W.S.; Lin, K.H.; Pan, P.S.; Kuo, Y.C.; Hsu, S.M.; Chen, J.K.; Wang, C.W.; Chen, K.H.; et al. Boron Neutron Capture Therapy: A New Generation of Targeted Charged-Particle Radiotherapy. *J. Sci. Tech. Res.* **2019**, *13*, 9687–9689. [CrossRef]
4. Turkez, H.; Arslan, M.E.; Tatar, A.; Mardinoglu, A. Promising potential of boron compounds against Glioblastoma: In Vitro antioxidant, anti-inflammatory and anticancer studies. *Neurochem. Int.* **2021**, *149*, 105137. [CrossRef] [PubMed]
5. Chio, C.M.; Huang, Y.C.; Chou, Y.C.; Hsu, F.C.; Lai, Y.B.; Yu, C.S. Boron Accumulation in Brain Tumor Cells through Boc-Protected Tryptophan as a Carrier for Boron Neutron Capture Therapy. *ACS Med. Chem. Lett.* **2020**, *11*, 589–596. [CrossRef] [PubMed]
6. Maslah, H.; Pethe, S.; Labruère, R. Boronic acid/boronate prodrugs for cancer treatment: Current status and perspectives. *Future Med. Chem.* **2021**, *13*, 859–861. [CrossRef]
7. Meiyanto, E.; Susidarti, R.; Jenie, R.; Utomo, R.; Novitasari, D.; Wulandari, F.; Kirihata, M. Synthesis of new boron containing compound (CCB-2) based on curcumin structure and its cytotoxic effect against cancer cells. *J. Appl. Pharm. Sci.* **2020**, *10*, 60–66.
8. Canturk, Z.; Tunali, Y.; Korkmaz, S.; Gulbaş, Z. Cytotoxic and apoptotic effects of boron compounds on leukemia cell line. *Cytotechnology* **2016**, *68*, 87–93. [CrossRef]
9. Koldemir-Gündüz, M.; Aydin, H.E.; Berikten, D.; Kaymak, G.; Köse, D.A.; Arslantaş, A. Synthesis of New Boron Derived Compounds; Anticancer, Antioxidant and Antimicrobial Effect in Vitro Glioblastoma Tumor Model. *J. Korean Neurosurg. Soc.* **2021**, *64*, 864–872. [CrossRef]
10. Song, S.; Gao, P.; Sun, L.; Kang, D.; Kongsted, J.; Poongavanam, V.; Zhan, P.; Liu, X. Recent developments in the medicinal chemistry of single boron atom-containing compounds. *Acta Pharm. Sin.* **2021**, *11*, 3035–3059. [CrossRef]
11. Franzyk, H.; Christensen, S.B. Targeting Toxins toward Tumors. *Molecules* **2021**, *26*, 1292. [CrossRef]
12. Kahraman, E.; Göker, E. Boric acid exert anti-cancer effect in poorly differentiated hepatocellular carcinoma cells via inhibition of AKT signaling pathway. *J. Trace Elem. Med. Biol.* **2022**, *73*, 127043. [CrossRef] [PubMed]
13. Sikora, A.; Zielonka, J.; Dębowska, K.; Michalski, R.; Smulik-Izydorczyk, R.; Pięta, J.; Podsiadły, R.; Artelska, A.; Pierzchała, K.; Kalyanaraman, B. Boronate-Based Probes for Biological Oxidants: A Novel Class of Molecular Tools for Redox Biology. *Front. Chem.* **2020**, *8*, 580899. [CrossRef] [PubMed]
14. Grzelakowska, A.; Modrzejewska, J.; Kolińska, J.; Szala, M.; Zielonka, M.; Dębowska, K.; Zakłos-Szyda, M.; Sikora, A.; Zielonka, J.; Podsiadły, R. Water-soluble cationic boronate probe based on coumarin imidazolium scaffold: Synthesis, characterization, and application to cellular peroxynitrite detection. *Free Radic. Biol. Med.* **2022**, *179*, 34–46. [CrossRef]
15. Zielonka, J.; Podsiadly, R.; Zielonka, M.; Hardy, M.; Kalyanaraman, B. On the use of peroxy-caged luciferin (PCL-1) probe for bioluminescent detection of inflammatory oxidants in vitro and in vivo—Identification of reaction intermediates and oxidant-specific minor products. *Free Radical. Biol. Med.* **2016**, *99*, 32–42. [CrossRef]
16. Cheng, G.; Pan, J.; Podsiadly, R.; Zielonka, J.; Garces, A.M.; Dias Duarte Machado, L.G.; Bennett, B.; McAllister, D.; Dwinell, M.B.; You, M.; et al. Increased formation of reactive oxygen species during tumor growth: Ex vivo low-temperature EPR and in vivo bioluminescence analyses. *Free Radic. Biol. Med.* **2020**, *147*, 167–174. [CrossRef] [PubMed]
17. Kuivila, H.G. Electrophilic Displacement Reactions. III. Kinetics of the Reaction between Hydrogen Peroxide and Benzeneboronic Acid1. *J. Am. Chem. Soc.* **1954**, *76*, 870–874. [CrossRef]
18. Sikora, A.; Zielonka, J.; Lopez, M.; Dybala-Defratyka, A.; Joseph, J.; Marcinek, A.; Kalyanaraman, B. Reaction between peroxynitrite and boronates: EPR spin-trapping, HPLC Analyses, and quantum mechanical study of the free radical pathway. *Chem. Res. Toxicol.* **2011**, *24*, 687–697. [CrossRef]
19. Sikora, A.; Zielonka, J.; Adamus, J.; Debski, D.; Dybala-Defratyka, A.; Michalowski, B.; Joseph, J.; Hartley, R.C.; Murphy, M.P.; Kalyanaraman, B. Reaction between peroxynitrite and triphenylphosphonium-substituted arylboronic acid isomers: Identification of diagnostic marker products and biological implications. *Chem. Res. Toxicol.* **2013**, *26*, 856–867. [CrossRef]
20. Van De Bittner, G.C.; Dubikovskaya, E.A.; Bertozzi, C.R.; Chang, C.J. In vivo imaging of hydrogen peroxide production in a murine tumor model with a chemoselective bioluminescent reporter. *Proc. Natl. Acad. Sci. USA* **2010**, *107*, 21316–21321. [CrossRef]
21. Carroll, V.; Michel, B.W.; Blecha, J.; VanBrocklin, H.; Keshari, K.; Wilson, D.; Chang, C.J. A Boronate-Caged [18F]FLT Probe for Hydrogen Peroxide Detection Using Positron Emission Tomography. *J. Am. Chem. Soc.* **2014**, *136*, 14742–14745. [CrossRef]
22. Lippert, A.R.; Van de Bittner, G.C.; Chang, C.J. Boronate oxidation as a bioorthogonal reaction approach for studying the chemistry of hydrogen peroxide in living systems. *Acc. Chem. Res.* **2011**, *44*, 793–804. [CrossRef] [PubMed]
23. Zielonka, J.; Zielonka, M.; Sikora, A.; Adamus, J.; Joseph, J.; Hardy, M.; Ouari, O.; Dranka, B.P.; Kalyanaraman, B. Global profiling of reactive oxygen and nitrogen species in biological systems: High-throughput real-time analyses. *J. Biol. Chem.* **2012**, *287*, 2984–2995. [CrossRef] [PubMed]
24. Zielonka, J.; Sikora, A.; Hardy, M.; Joseph, J.; Dranka, B.P.; Kalyanaraman, B. Boronate probes as diagnostic tools for real time monitoring of peroxynitrite and hydroperoxides. *Chem. Res. Toxicol.* **2012**, *25*, 1793–1799. [CrossRef] [PubMed]

25. Zielonka, J.; Sikora, A.; Joseph, J.; Kalyanaraman, B. Peroxynitrite is the major species formed from different flux ratios of co-generated nitric oxide and superoxide: Direct reaction with boronate-based fluorescent probe. *J. Biol. Chem.* **2010**, *285*, 14210–14216. [CrossRef] [PubMed]
26. Rios, N.; Radi, R.; Kalyanaraman, B.; Zielonka, J. Tracking isotopically labeled oxidants using boronate-based redox probes. *J. Biol. Chem.* **2020**, *295*, 6665–6676. [CrossRef]
27. Sieracki, N.A.; Gantner, B.N.; Mao, M.; Horner, J.H.; Ye, R.D.; Malik, A.B.; Newcomb, M.E.; Bonini, M.G. Bioluminescent detection of peroxynitrite with a boronic acid-caged luciferin. *Free Radic. Biol. Med.* **2013**, *61*, 40–50. [CrossRef]
28. Kalyanaraman, B.; Hardy, M.; Podsiadly, R.; Cheng, G.; Zielonka, J. Recent developments in detection of superoxide radical anion and hydrogen peroxide: Opportunities, challenges, and implications in redox signaling. *Arch. Biochem. Biophys.* **2017**, *617*, 38–47. [CrossRef]
29. Maslah, H.; Skarbek, C.; Pethe, S.; Labruère, R. Anticancer boron-containing prodrugs responsive to oxidative stress from the tumor microenvironment. *Eur. J. Med. Chem.* **2020**, *207*, 112670. [CrossRef]
30. Jia, P.; Dai, C.; Cao, P.; Sun, D.; Ouyang, R.; Miao, Y. The role of reactive oxygen species in tumor treatment. *RSC Adv.* **2020**, *10*, 7740–7750. [CrossRef]
31. Wang, T.; Xu, H. Multi-faced roles of reactive oxygen species in anti-tumor T cell immune responses and combination immunotherapy. *Explor. Med.* **2022**, *3*, 77–98. [CrossRef]
32. Liu, R.; Peng, L.; Zhou, L.; Huang, Z.; Zhou, C.; Huang, C. Oxidative Stress in Cancer Immunotherapy: Molecular Mechanisms and Potential Applications. *Antioxidants* **2022**, *11*, 853. [CrossRef] [PubMed]
33. Kotsafti, A.; Scarpa, M.; Castagliuolo, I.; Scarpa, M. Reactive Oxygen Species and Antitumor Immunity-From Surveillance to Evasion. *Cancers* **2020**, *12*, 1748. [CrossRef] [PubMed]
34. Lian, X.; Yang, K.; Li, R.; Li, M.; Zuo, J.; Zheng, B.; Wang, W.; Wang, P.; Zhou, S. Immunometabolic rewiring in tumorigenesis and anti-tumor immunotherapy. *Mol. Cancer* **2022**, *21*, 27. [CrossRef] [PubMed]
35. Aboelella, N.S.; Brandle, C.; Kim, T.; Ding, Z.C.; Zhou, G. Oxidative Stress in the Tumor Microenvironment and Its Relevance to Cancer Immunotherapy. *Cancers* **2021**, *13*, 986. [CrossRef]
36. Gabrilovich, D.I.; Nagaraj, S. Myeloid-derived suppressor cells as regulators of the immune system. *Nat. Rev. Immunol.* **2009**, *9*, 162–174. [CrossRef]
37. Krishnamoorthy, M.; Gerhardt, L.; Maleki Vareki, S. Immunosuppressive Effects of Myeloid-Derived Suppressor Cells in Cancer and Immunotherapy. *Cells* **2021**, *10*, 1170. [CrossRef]
38. Lu, T.; Ramakrishnan, R.; Altiok, S.; Youn, J.I.; Cheng, P.; Celis, E.; Pisarev, V.; Sherman, S.; Sporn, M.B.; Gabrilovich, D. Tumor-infiltrating myeloid cells induce tumor cell resistance to cytotoxic T cells in mice. *J. Clin. Invest.* **2011**, *121*, 4015–4029. [CrossRef]
39. Buck, M.D.; O'Sullivan, D.; Pearce, E.L. T cell metabolism drives immunity. *J. Exp. Med.* **2015**, *212*, 1345–1360. [CrossRef]
40. De Sanctis, F.; Lamolinara, A.; Boschi, F.; Musiu, C.; Caligola, S.; Trovato, R.; Fiore, A.; Frusteri, C.; Anselmi, C.; Poffe, O.; et al. Interrupting the nitrosative stress fuels tumor-specific cytotoxic T lymphocytes in pancreatic cancer. *J. Immunother. Cancer* **2022**, *10*, e003549. [CrossRef]
41. Molon, B.; Ugel, S.; Del Pozzo, F.; Soldani, C.; Zilio, S.; Avella, D.; De Palma, A.; Mauri, P.; Monegal, A.; Rescigno, M.; et al. Chemokine nitration prevents intratumoral infiltration of antigen-specific T cells. *J. Exp. Med.* **2011**, *208*, 1949–1962. [CrossRef]
42. Olivier, C.; Oliver, L.; Lalier, L.; Vallette, F.M. Drug Resistance in Glioblastoma: The Two Faces of Oxidative Stress. *Front. Mol. Biosci.* **2020**, *7*, 620677. [CrossRef] [PubMed]
43. Pan, J.; Lee, Y.; Cheng, G.; Zielonka, J.; Zhang, Q.; Bajzikova, M.; Xiong, D.; Tsaih, S.W.; Hardy, M.; Flister, M.; et al. Mitochondria-Targeted Honokiol Confers a Striking Inhibitory Effect on Lung Cancer via Inhibiting Complex I Activity. *iScience* **2018**, *3*, 192–207. [CrossRef] [PubMed]
44. Cheng, G.; Hardy, M.; Zielonka, J.; Weh, K.M.; Zielonka, M.; Boyle, K.; Abu Eid, M.; McAllister, D.; Bennett, B.; Kresty, L.A.; et al. Mitochondria-Targeted Magnolol Inhibits OXPHOS, Proliferation, and Tumor Growth via Modulation of Energetics and Autophagy in Melanoma Cells. *Cancer Res. Treat. Commun.* **2020**, *25*, 100210. [CrossRef]
45. Cheng, G.; Hardy, M.; Topchyan, P.; Zander, R.; Volberding, P.; Cui, W.; Kalyanaraman, B. Potent inhibition of tumour cell proliferation and immunoregulatory function by mitochondria-targeted atovaquone. *Sci. Rep.* **2020**, *10*, 17872. [CrossRef] [PubMed]
46. Cheng, G.; Zielonka, J.; Ouari, O.; Lopez, M.; McAllister, D.; Boyle, K.; Barrios, C.S.; Weber, J.J.; Johnson, B.D.; Hardy, M.; et al. Mitochondria-Targeted Analogues of Metformin Exhibit Enhanced Antiproliferative and Radiosensitizing Effects in Pancreatic Cancer Cells. *Cancer Res.* **2016**, *76*, 3904–3915. [CrossRef]
47. Viswanadhan, V.N.; Ghose, A.K.; Revankar, G.R.; Robins, R.K. Atomic physicochemical parameters for three dimensional structure directed quantitative structure-activity relationships. 4. Additional parameters for hydrophobic and dispersive interactions and their application for an automated superposition of certain naturally occurring nucleoside antibiotics. *J. Chem. Inf. Comput. Sci.* **1989**, *29*, 163–172.
48. Klopman, G.; Li, J.-Y.; Wang, S.; Dimayuga, M. Computer Automated log P Calculations Based on an Extended Group Contribution Approach. *J. Chem. Inf. Comput. Sci.* **1994**, *34*, 752–781. [CrossRef]
49. Bohle, D.S.; Glassbrenner, P.A.; Hansert, B. Syntheses of pure tetramethylammonium peroxynitrite. *Methods Enzymol.* **1996**, *269*, 302–311.

50. Szala, M.; Grzelakowska, A.; Modrzejewska, J.; Siarkiewicz, P.; Słowiński, D.; Świerczyńska, M.; Zielonka, J.; Podsiadły, R. Characterization of the reactivity of luciferin boronate—A probe for inflammatory oxidants with improved stability. *Dye. Pigment.* **2020**, *183*, 108693. [CrossRef]
51. Sikora, A.; Zielonka, J.; Lopez, M.; Joseph, J.; Kalyanaraman, B. Direct oxidation of boronates by peroxynitrite: Mechanism and implications in fluorescence imaging of peroxynitrite. *Free Radical Biol. Med.* **2009**, *47*, 1401–1407. [CrossRef]
52. Huang, M.; Xiong, D.; Pan, J.; Zhang, Q.; Wang, Y.; Myers, C.R.; Johnson, B.D.; Hardy, M.; Kalyanaraman, B.; You, M. Prevention of Tumor Growth and Dissemination by In Situ Vaccination with Mitochondria-Targeted Atovaquone. *Adv. Sci.* **2022**, *9*, 2101267. [CrossRef] [PubMed]
53. AbuEid, M.; McAllister, D.M.; McOlash, L.; Harwig, M.C.; Cheng, G.; Drouillard, D.; Boyle, K.A.; Hardy, M.; Zielonka, J.; Johnson, B.D.; et al. Synchronous effects of targeted mitochondrial complex I inhibitors on tumor and immune cells abrogate melanoma progression. *iScience* **2021**, *24*, 102653. [CrossRef] [PubMed]
54. Zhang, Q.; Xiong, D.; Pan, J.; Wang, Y.; Hardy, M.; Kalyanaraman, B.; You, M. Chemoprevention of Lung Cancer with a Combination of Mitochondria-Targeted Compounds. *Cancers* **2022**, *14*, 2538. [CrossRef]
55. Corzo, C.A.; Cotter, M.J.; Cheng, P.; Cheng, F.; Kusmartsev, S.; Sotomayor, E.; Padhya, T.; McCaffrey, T.V.; McCaffrey, J.C.; Gabrilovich, D.I. Mechanism regulating reactive oxygen species in tumor-induced myeloid-derived suppressor cells. *J. Immunol.* **2009**, *182*, 5693–5701. [CrossRef] [PubMed]
56. Langley, M.; Ghosh, A.; Charli, A.; Sarkar, S.; Ay, M.; Luo, J.; Zielonka, J.; Brenza, T.; Bennett, B.; Jin, H.; et al. Mito-Apocynin Prevents Mitochondrial Dysfunction, Microglial Activation, Oxidative Damage, and Progressive Neurodegeneration in MitoPark Transgenic Mice. *Antioxid. Redox Signal.* **2017**, *27*, 1048–1066. [CrossRef] [PubMed]
57. Ghosh, A.; Langley, M.R.; Harischandra, D.S.; Neal, M.L.; Jin, H.; Anantharam, V.; Joseph, J.; Brenza, T.; Narasimhan, B.; Kanthasamy, A.; et al. Mitoapocynin Treatment Protects Against Neuroinflammation and Dopaminergic Neurodegeneration in a Preclinical Animal Model of Parkinson's Disease. *J. Neuroimmune Pharmacol.* **2016**, *11*, 259–278. [CrossRef] [PubMed]
58. Mukhopadhyay, P.; Horvath, B.; Zsengeller, Z.; Zielonka, J.; Tanchian, G.; Holovac, E.; Kechrid, M.; Patel, V.; Stillman, I.E.; Parikh, S.M.; et al. Mitochondrial-targeted antioxidants represent a promising approach for prevention of cisplatin-induced nephropathy. *Free Radic. Biol. Med.* **2012**, *52*, 497–506. [CrossRef] [PubMed]
59. Zielonka, J.; Zielonka, M.; VerPlank, L.; Cheng, G.; Hardy, M.; Ouari, O.; Ayhan, M.M.; Podsiadly, R.; Sikora, A.; Lambeth, J.D.; et al. Mitigation of NADPH oxidase 2 activity as a strategy to inhibit peroxynitrite formation. *J. Biol. Chem.* **2016**, *291*, 7029–7044. [CrossRef]
60. Ford, K.; Hanley, C.J.; Mellone, M.; Szyndralewiez, C.; Heitz, F.; Wiesel, P.; Wood, O.; Machado, M.; Lopez, M.A.; Ganesan, A.P.; et al. NOX4 Inhibition Potentiates Immunotherapy by Overcoming Cancer-Associated Fibroblast-Mediated CD8 T-cell Exclusion from Tumors. *Cancer Res.* **2020**, *80*, 1846–1860. [CrossRef]
61. Konaté, M.M.; Antony, S.; Doroshow, J.H. Inhibiting the Activity of NADPH Oxidase in Cancer. *Antioxid. Redox Signal.* **2020**, *33*, 435–454. [CrossRef]
62. Chung, A.W.; Anand, K.; Anselme, A.C.; Chan, A.A.; Gupta, N.; Venta, L.A.; Schwartz, M.R.; Qian, W.; Xu, Y.; Zhang, L.; et al. A phase 1/2 clinical trial of the nitric oxide synthase inhibitor L-NMMA and taxane for treating chemoresistant triple-negative breast cancer. *Sci. Transl. Med.* **2021**, *13*, eabj5070. [CrossRef] [PubMed]
63. Adebayo, A.K.; Nakshatri, H. Modeling preclinical cancer studies under physioxia to enhance clinical translation. *Cancer Res.* **2022**, *82*, 4313–4321. [CrossRef] [PubMed]
64. University of Oxford. Atovaquone as Tumour HypOxia Modifier (ATOM). ClinicalTrials.gov identifier: NCT02628080. Updated 4 September 2019. Available online: https://clinicaltrials.gov/ct2/show/NCT02628080 (accessed on 21 December 2022).
65. Skwarski, M.; McGowan, D.R.; Belcher, E.; Di Chiara, F.; Stavroulias, D.; McCole, M.; Derham, J.L.; Chu, K.Y.; Teoh, E.; Chauhan, J.; et al. Mitochondrial Inhibitor Atovaquone Increases Tumor Oxygenation and Inhibits Hypoxic Gene Expression in Patients with Non-Small Cell Lung Cancer. *Clin. Cancer. Res.* **2021**, *27*, 2459–2469. [CrossRef] [PubMed]
66. Bourigault, P.; Skwarski, M.; Macpherson, R.E.; Higgins, G.S.; McGowan, D.R. Investigation of atovaquone-induced spatial changes in tumour hypoxia assessed by hypoxia PET/CT in non-small cell lung cancer patients. *EJNMMI Res.* **2021**, *11*, 130. [CrossRef]
67. Kalyanaraman, B.; Cheng, G.; Hardy, M. Therapeutic Targeting of Tumor Cells and Tumor Immune Microenvironment Vulnerabilities. *Front. Oncol.* **2022**, *12*, 816504. [CrossRef] [PubMed]
68. Kalyanaraman, B. Exploiting the tumor immune microenvironment and immunometabolism using mitochondria-targeted drugs: Challenges and opportunities in racial disparity and cancer outcome research. *FASEB J.* **2022**, *36*, e22226. [CrossRef] [PubMed]
69. Piyarathna, D.W.B.; Balasubramanian, A.; Arnold, J.M.; Lloyd, S.M.; Karanam, B.; Castro, P.; Ittmann, M.M.; Putluri, N.; Navone, N.; Jones, J.A.; et al. ERR1 and PGC1α associated mitochondrial alterations correlate with pan-cancer disparity in African Americans. *J. Clin. Invest.* **2019**, *129*, 2351–2356. [CrossRef]
70. Choudhury, A.R.; Singh, K.K. Mitochondrial determinants of cancer health disparities. *Semin. Cancer Biol.* **2017**, *47*, 125–146. [CrossRef]
71. Reddy, K.R.K.; Park, J.H.; Bollag, R.J.; Bellman, A.; Terris, M.; Lerner, S.P.; Ballester, L.Y.; Lotan, Y.; Kaipparettu, B.A.; Putluri, N. Abstract 3771: Mitochondrial metabolism and racial disparity of bladder cancer. *Cancer Res.* **2022**, *82*, 3771. [CrossRef]
72. Kim, G.; Pastoriza, J.M.; Condeelis, J.S.; Sparano, J.A.; Filippou, P.S.; Karagiannis, G.S.; Oktay, M.H. The Contribution of Race to Breast Tumor Microenvironment Composition and Disease Progression. *Front. Oncol.* **2020**, *10*, 1022. [CrossRef]

73. Yaghoobi, V.; Moutafi, M.; Aung, T.N.; Pelekanou, V.; Yaghoubi, S.; Blenman, K.; Ibrahim, E.; Vathiotis, I.A.; Shafi, S.; Sharma, A.; et al. Quantitative assessment of the immune microenvironment in African American Triple Negative Breast Cancer: A case-control study. *Breast Cancer Res.* **2021**, *23*, 113. [CrossRef] [PubMed]
74. Abdou, Y.; Attwood, K.; Cheng, T.D.; Yao, S.; Bandera, E.V.; Zirpoli, G.R.; Ondracek, R.P.; Stein, L.; Bshara, W.; Khoury, T.; et al. Racial differences in CD8(+) T cell infiltration in breast tumors from Black and White women. *Breast Cancer Res.* **2020**, *22*, 62. [CrossRef] [PubMed]
75. Yao, S.; Cheng, T.D.; Elkhanany, A.; Yan, L.; Omilian, A.; Abrams, S.I.; Evans, S.; Hong, C.C.; Qi, Q.; Davis, W.; et al. Breast Tumor Microenvironment in Black Women: A Distinct Signature of CD8+ T-Cell Exhaustion. *J. Natl. Cancer Inst.* **2021**, *113*, 1036–1043. [CrossRef] [PubMed]
76. Beebe-Dimmer, J.L.; Cooney, K.A. Mitochondrial alterations may underlie race-specific differences in cancer risk and outcome. *J. Clin. Invest.* **2019**, *129*, 2187–2188. [CrossRef] [PubMed]
77. Williams, L.K.; Padhukasahasram, B.; Ahmedani, B.K.; Peterson, E.L.; Wells, K.E.; González Burchard, E.; Lanfear, D.E. Differing effects of metformin on glycemic control by race-ethnicity. *J. Clin. Endocrinol. Metab.* **2014**, *99*, 3160–3168. [CrossRef]
78. Weinberg, S.E.; Chandel, N.S. Targeting mitochondria metabolism for cancer therapy. *Nat. Chem. Biol.* **2015**, *11*, 9–15. [CrossRef]
79. Vyas, S.; Zaganjor, E.; Haigis, M.C. Mitochondria and cancer. *Cell* **2016**, *166*, 555–566. [CrossRef]
80. Xu, Y.; Xue, D.; Bankhead, A., 3rd; Neamati, N. Why All the Fuss about Oxidative Phosphorylation (OXPHOS)? *J. Med. Chem.* **2020**, *63*, 14276–14307. [CrossRef]
81. Chandel, N. S Mitochondria: Back to the future. *Nat. Rev. Mol. Cell Biol.* **2018**, *19*, 76. [CrossRef]
82. Cheng, G.; Hardy, M.; You, M.; Kalyanaraman, B. Combining PEGylated mito-atovaquone with MCT and Krebs cycle redox inhibitors as a potential strategy to abrogate tumor cell proliferation. *Sci. Rep.* **2022**, *12*, 5143. [CrossRef]
83. Evans, K.W.; Yuca, E.; Scott, S.S.; Zhao, M.; Paez Arango, N.; Cruz Pico, C.X.; Saridogan, T.; Shariati, M.; Class, C.A.; Bristow, C.A.; et al. Oxidative Phosphorylation Is a Metabolic Vulnerability in Chemotherapy-Resistant Triple-Negative Breast Cancer. *Cancer Res.* **2021**, *81*, 5572–5581. [CrossRef] [PubMed]